https://doi.org/10.5194/egusphere-2026-1110
Preprint. Discussion started: 13 March 2026

Role of ionospheric and ground contributions in driving GIC: Northern Europe at the peak of the May 2024 superstorm

Liisa Juusola[1], Ari Viljanen[1], Ilja Honkonen[1], Magnar Gullikstad Johnsen[2], Andrew Dimmock[3], Vanina Lanabere[3], and Alice Wallner[3]

[1]Finnish Meteorological Institute, Helsinki, Finland.
[2]Tromsø Geophysical Observatory, UiT The Arctic University of Norway, Tromsø, Norway.
[3]Swedish Institute of Space Physics, Uppsala, Sweden.

Correspondence: Liisa Juusola (liisa.juusola@fmi.fi)

Abstract. We examine the geoelectric field and geomagnetically induced current (GIC) in Northern Europe during the May 2024 superstorm using a recently developed method: The divergence-free part of the geoelectric field ($\boldsymbol{E}_{DF}$), associated with rapid magnetic field variations, is estimated from ground-based magnetic field observations using spherical elementary current systems. The curl-free part of the geoelectric field ($\boldsymbol{E}_{CF}$), associated with charge accumulation, is estimated from $\boldsymbol{E}_{DF}$ using coefficients that depend on ground conductivity and linearly relate $\boldsymbol{E}_{CF}$ to $\boldsymbol{E}_{DF}$ in the time domain. We apply the method to both regional 10 s International Monitor for Auroral Geomagnetic Effects (IMAGE) magnetometer observations and global 1 min SuperMAG observations by adopting a global triangular grid adapted to local magnetometer density. We compare the resulting GIC in the Finnish benchmark power grid and conclude that, in the absence of ground conductivity information and higher cadence data, $\boldsymbol{E}_{DF}$ estimated from 1 min magnetic field observations alone can provide a reasonable proxy for GIC activity in a power grid compared to 10 s geoelectric field. However, polarization of the geoelectric field due to lateral variations in ground conductivity can produce intense GIC at substations connected to transmission lines traversing regions of enhanced geoelectric field. GIC at such substations may be poorly described by $\boldsymbol{E}_{DF}$ alone.

1 Introduction

The geoelectric field at the Earth's surface drives potentially hazardous geomagnetically induced currents (GIC) in grounded technological conductor networks, such as electric power transmission grids (Pulkkinen et al., 2017). Recently, Rosenqvist et al. (2025) have analysed a comprensive list of disturbances reported in the Swedish power grid between 1999 and June 2024. They showed a clear increase in the occurrence rate of incidents for high geomagnetic activity. Their list of disturbances classified as related to GIC includes the Malmö blackout during the October 2003 storm. The most recent occurrence on the list, disconnection of the SwePol high voltage direct-current link between Sweden and Poland, took place in Karlshamn during the May 2024 geomagnetic superstorm. Various aspects of the May 2024 storm have been studied for example by Gonzalez-Esparza et al. (2024); Michelis and Consolini (2025); Fu et al. (2025); Lawrence et al. (2025); Mac Manus et al. (2025); Ohtani et al. (2025); Piersanti et al. (2025); Weiler et al. (2025). The storm also caused the tripping of a high voltage transformer in the county of Trøndelag in Norway, without causing any wide spread blackouts (internal communication).

https://doi.org/10.5194/egusphere-2026-1110
Preprint. Discussion started: 13 March 2026

The time derivative of the ground-based magnetic field ($d\boldsymbol{B}/dt$) has often been used as a proxy for the GIC risk (Viljanen, 1998; Viljanen et al., 2001). GIC estimates for a fixed configuration of a particular conductor system based on empirical relations to components of $d\boldsymbol{B}/dt$ or frequency domain filtered components of $\boldsymbol{B}$ have also been widely used (see, e.g., Marshall et al., 2011; Kelbert, 2020). A preferable approach, however, is to calculate GIC in the conductor system based on a known geoelectric field and a direct current model of the system, such as power grid or pipeline (Lehtinen and Pirjola, 1985; Viljanen et al., 2012; Boteler, 2013; Viljanen et al., 2014; Kelly et al., 2017; Pirjola et al., 2022).

Because dense and continuously operating magnetotelluric (MT) networks are not available (e.g., Kelbert, 2020; Lyon et al., 2025), the geoelectric field is typically estimated from ground-based magnetic field observations. In first-principle methods (Honkonen et al., 2018; Rosenqvist and Hall, 2019; Marshalko et al., 2021; Kruglyakov et al., 2022; Marshalko et al., 2023; Kruglyakov et al., 2023), the external driver, i.e., ground-based magnetic field variations obtained either from observations or magnetosphere-ionosphere simulations, and the 3-D ground conductivity are given as input, and the geoelectric field is obtained as a solution to the Maxwell equations. This approach can be computationally expensive but has recently become feasible. The underlying conductivity model is the source of the largest uncertainty in the resulting geoelectric field. In empirical modelling, the geoelectric field is typically estimated from ground-based magnetic field observations using 3-D MT impedances (Kelbert et al., 2017; Love et al., 2018; Lucas et al., 2020; Malone-Leigh et al., 2023). This method requires an implicit plane wave assumption for the external source and there are issues related to the spatial representativeness of the impedances (Cordell et al., 2021; Murphy et al., 2021; Malone-Leigh et al., 2024).

A different approach to empirical geoelectric field modelling was recently presented by Juusola et al. (2025b). The technique is based on separating the geoelectric field on the ground into divergence-free (DF) and curl-free (CF) parts. $\boldsymbol{E}_{DF}$ is associated with geomagnetic field variations, produced by external electric currents in the ionosphere and magnetosphere and internal induced telluric currents in the conducting ground, according to Faraday's law

$$\nabla \times \boldsymbol{E}_{DF} = -\frac{\partial \boldsymbol{B}}{\partial t}. \tag{1}$$

$\boldsymbol{E}_{CF}$ is associated with the electric charge density ρ, accumulated at ground conductivity gradients, according to Gauss's law

$$\nabla \cdot \boldsymbol{E}_{CF} = \frac{\rho}{\epsilon_0}, \tag{2}$$

where ϵ_0 is the vacuum permittivity. The charge accumulation is driven by $\boldsymbol{E}_{DF}$ according to the requirement of telluric current continuity. The total geoelectric field is the sum of these two contributions

$$\boldsymbol{E} = \boldsymbol{E}_{DF} + \boldsymbol{E}_{CF}. \tag{3}$$

$\boldsymbol{E}_{DF}$ is estimated from ground-based magnetic field observations using spherical elementary current systems (SECS) (Amm, 1997; Amm and Viljanen, 1999; Pulkkinen et al., 2003a, b; McLay and Beggan, 2010; Weygand et al., 2011; Juusola et al., 2016; Marsal et al., 2017, 2020; Juusola et al., 2020; Laundal et al., 2021; Vanhamäki and Juusola, 2020; Juusola et al., 2023a, b, 2025b). The only input needed to estimate $\boldsymbol{E}_{DF}$ are magnetic field observations. The ground conductivity naturally affects the telluric current distribution through ρ and $\boldsymbol{E}_{CF}$, and thus information on the ground conductivity is included in the

https://doi.org/10.5194/egusphere-2026-1110
Preprint. Discussion started: 13 March 2026

internal geomagnetic variations. The resulting $\boldsymbol{E}_{DF}$ represent the large-scale geoelectric field because small-scale "distortions" by electric charges have been eliminated. Because no conductivity model is needed in the calculation, the largest uncertainty is associated with sparse magnetometer coverage. The method preserves spatial variations of the external source and is computationally feasible for near-real time operations as well. In case subsurface conductivity models or MT impedances are not available, $\boldsymbol{E}_{DF}$ may provide a reasonable substitute to $\boldsymbol{E}$, since geomagnetic recordings are quite extensively available. The method produces ionospheric equivalent currents as well, and thus provides information on the external driver. $\boldsymbol{E}_{CF}$ is estimated from $\boldsymbol{E}_{DF}$ according to a simple linear relationship in the time domain. The conductivity model used in the derivation of the involved coefficients contributes to the uncertainty of $\boldsymbol{E}_{CF}$.

We will apply the Juusola et al. (2025b) method to study the contributions from $\boldsymbol{E}_{DF}$ and $\boldsymbol{E}_{CF}$ in driving GIC. Simultaneous magnetic and electric field measurements have been observed to exhibit orders of magnitude greater spatial variability in the electric field than in the magnetic field measurements, suggesting that charge accumulation at ground conductivity gradients plays a key role in governing the spatial variability of the geoelectric field (Kelbert, 2020; Cordell et al., 2025). The charges can cause partial polarization of the geoelectric field (e.g., Liu et al., 2019) such that its direction can differ greatly from the direction of the external geoelectric field. Calculating GIC in a power grid involves integration of the geoelectric field along the power lines. Any transmission lines parallel to the polarization direction will then have larger voltages than lines perpendicular to the polarization direction (Cordell et al., 2021; Malone-Leigh et al., 2024). Although the geoelectric field structures produced by charges can be very intense, they also tend to have small scale-sizes, at least in Fennoscandia (Marshalko et al., 2023). To what extent the smoothing effect of the integration of the geoelectric field might diminish the role of small-scale geoelectric field structures in driving GIC has not been satisfactorily settled (Kelbert, 2020). Related to this question, we will examine if $\boldsymbol{E}_{DF}$ can provide a good proxy for general GIC level. We will further develop the equivalent current density and $\boldsymbol{E}_{DF}$ calculation by replacing the rectangular grid typically used in SECS analysis with a global triangular grid where the grid cell size and density is adapted to local magnetometer density. Such a grid allows robust derivation of global equivalent current and $\boldsymbol{E}_{DF}$ maps with more detail produced in areas densely covered by magnetometers and only large-scale features obtained for areas with few observations. The structure of the study is as follows: the data and methods are described in Section 2, the results are presented in Section 3 and discussed in Section 4. The conlusions are summarised in Section 5.

2 Data and methods

2.1 Geomagnetic and geoelectric field observations

We have used ground magnetic field measurements from the International Monitor for Auroral Geomagnetic Effects (IMAGE) magnetometer network (Juusola et al., 2025a) and SuperMAG magnetometer data repository (Gjerloev, 2012). IMAGE is a regional variometer array located in northern Europe that provides vector magnetic field observations at 10 s cadence. After correcting the data for any erroneous spikes and jumps, a 10-day sliding median baseline was subtracted from the data. SuperMAG provides global observations at 1 min cadence, and the subtracted baseline is described by Gjerloev (2012). IMAGE magnetometers also provide data to SuperMAG. After the baseline subtraction, the remaining magnetic field variations consist

https://doi.org/10.5194/egusphere-2026-1110
Preprint. Discussion started: 13 March 2026

of an external part mainly due to ionospheric electric currents but with some magnetospheric contribution as well, and an internal part due to induced telluric currents in the conducting ground.

The Baltic Electromagnetic Array Research (BEAR) network (Korja et al., 2002) operated in Fennoscandia during June-July 1998 for about 1.5 months, recording magnetic and electric fields in a denser network than IMAGE. We utilize 10 s magnetic and electric field data from BEAR. From the magnetic field data, the baseline was subtracted similar to IMAGE data. From the electric field data, the median value of the event was subtracted to account for instrumental offset.

2.2 Equivalent current density and modelled divergence-free geoelectric field

Rapid geomagnetic variations observed by ground-based magnetometers are caused by variations in three-dimensional (3-D) ionospheric and magnetospheric electric currents above 90 km altitude and by variations in 3-D induced telluric currents below the Earth's surface. The three vector components of these magnetic field variations between the ground and the bottom of the space current region can be conveniently described by two spherical layers of DF sheet currents, called equivalent currents (Haines and Torta, 1994), placed at the top of the telluric current region (directly below the Earth's surface) and at the bottom of the space current region (90 km altitude).

We have used the SECS method (Juusola et al., 2025b) to calculate the ionospheric and telluric equivalent current density ($\boldsymbol{J}_{eq}$) and ground $\boldsymbol{E}_{DF}$ from observations of the magnetic field variation. DF 2-D SECS poles were placed at 1 m depth and at 90 km altitude on a global triangular grid adapted to local magnetometer density, as described in Appendix A. Each SECS has an amplitude (I_{DF}), and these amplitudes were determined by fitting the superposed magnetic field of the SECSs to the three components of the measured magnetic field (Vanhamäki and Juusola, 2020). The time derivative of the SECS amplitudes was calculated as

$$\frac{\partial I_{DF}}{\partial t} = \frac{I_{DF}(t) - I_{DF}(t-\Delta t)}{\Delta t}, \tag{4}$$

where Δt is the time step of the data. $\boldsymbol{E}_{DF}$ associated with $\partial \boldsymbol{B}/\partial t$ (Eq. 1) was calculated from $\partial I_{DF}/\partial t$ as described by Juusola et al. (2025b, section 2.2). The external part of $\boldsymbol{E}_{DF}$ was obtained from the ionospheric $\partial I_{DF}/\partial t$, and the internal part of $\boldsymbol{E}_{DF}$ was obtained from the telluric $\partial I_{DF}/\partial t$. The total $\boldsymbol{E}_{DF}$ was calculated as a vector sum of the external and internal parts.

Figure 1a–c shows examples of the ionospheric equivalent current density $\boldsymbol{J}_{eq}$ and ground $\boldsymbol{E}_{DF}$ derived from BEAR, IMAGE, and SuperMAG magnetometer observations on 26 June 1998 at 03:23:00 UT. In June 1998, IMAGE network was very sparse, consisting only of 21 stations. The number of IMAGE stations has increased over the years, and reached 56 in the latest expansion in October 2022. The number of stations providing data to SuperMAG has increased since 1998 as well. In each panel of Fig. 1, the key arrow length has been set according to the maximum value in each plot. Despite the differences in station distribution, the $\boldsymbol{J}_{eq}$ and $\boldsymbol{E}_{DF}$ patterns and amplitudes in Fennoscandia are quite similar in Fig. 1a–c and in Fig. 1d–e. The amplitude of SuperMAG $\boldsymbol{E}_{DF}$ (Fig. 1f) is somewhat lower than those of IMAGE and BEAR $\boldsymbol{E}_{DF}$ (Fig. 1d–e), due to being derived from 1 min instead of 10 s data (cf. Pulkkinen et al., 2006). In summary, Fig. 1 demonstrates that the combination of the SECS method and adaptable triangular grid is scalable to different magnetometer configurations.

https://doi.org/10.5194/egusphere-2026-1110
Preprint. Discussion started: 13 March 2026

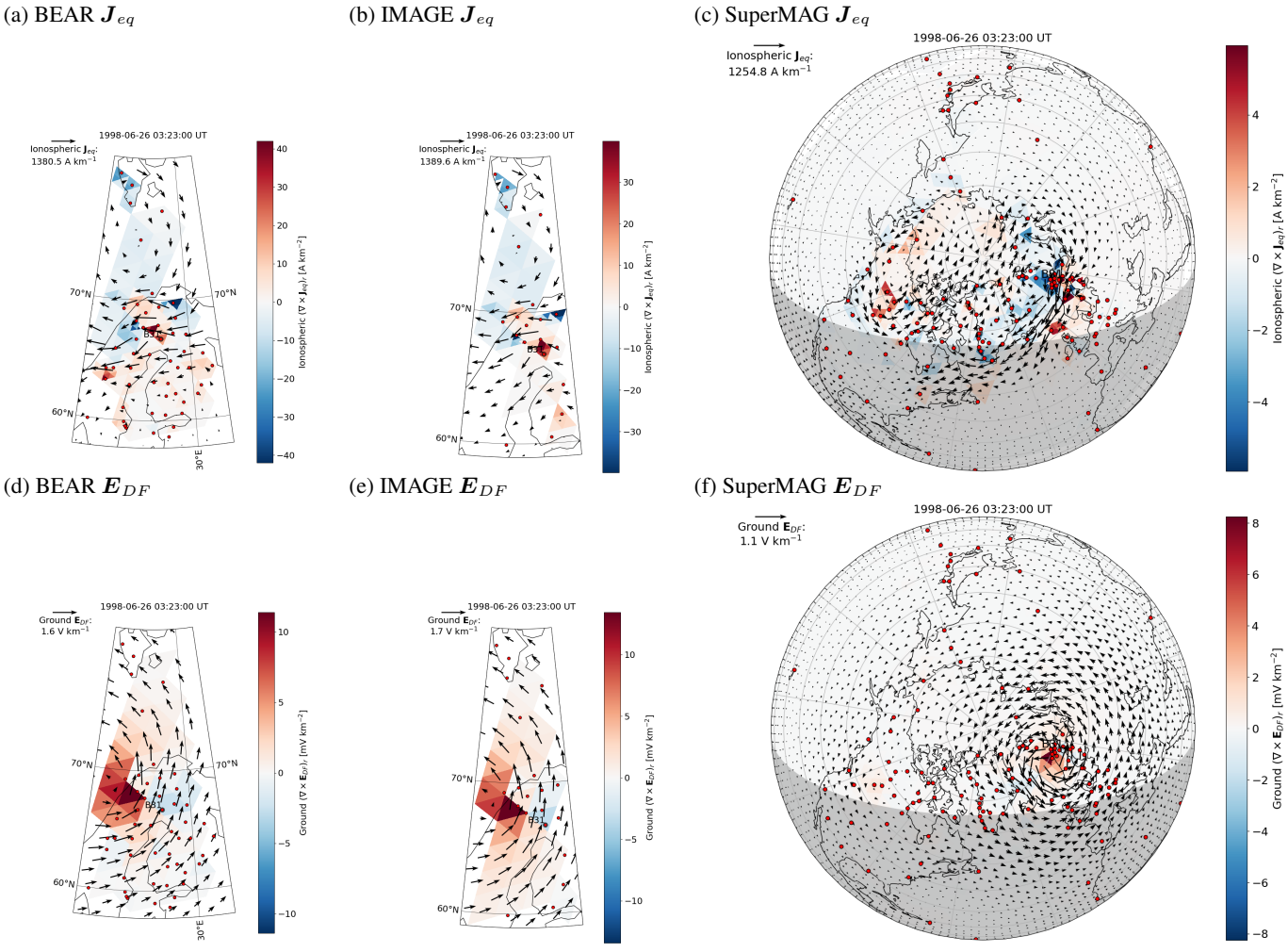

Figure 1. (a): Ionospheric equivalent current density ($\boldsymbol{J}_{eq}$, arrows) and its curl ($(\nabla \times \boldsymbol{J}_{eq})_r$, color) on 26 June 1998 at 03:23:00 UT, derived from 10 s BEAR magnetometer observations (red dots). (b): $\boldsymbol{J}_{eq}$ derived from 10 s IMAGE magnetometer observations. (c): $\boldsymbol{J}_{eq}$ derived from 1 min SuperMAG magnetometer observations. (d): Divergence-free part of the electric field on the ground ($\boldsymbol{E}_{DF}$, arrows) and its curl ($(\nabla \times \boldsymbol{E}_{DF})_r$, color), derived from BEAR magnetometer observations. (e): $\boldsymbol{E}_{DF}$ derived from IMAGE observations. (f): $\boldsymbol{E}_{DF}$ derived from SuperMAG observations. The scale arrow shows the maximum value of the quantity of each plot.

2.3 Modelled total geoelectric field

In addition to $\boldsymbol{E}_{DF}$ (Eq. 1), the total geoelectric field at the Earth's surface includes $\boldsymbol{E}_{CF}$ (Eq. 2–3), created by charge accumulation at ground conductivity gradients. Whereas $\boldsymbol{E}_{DF}$ can be calculated without any direct information on ground conductivity, such information is required for deriving $\boldsymbol{E}_{CF}$. We use the method derived by Juusola et al. (2025b), where $\boldsymbol{E}_{CF}$

https://doi.org/10.5194/egusphere-2026-1110
Preprint. Discussion started: 13 March 2026

is assumed to be proportional to $\boldsymbol{E}_{DF}$

$$E_{CF,x}(t, r = R_E, \theta, \phi) = k_{xx}(r = R_E, \theta, \phi) E_{DF,x}(t, r = R_E, \theta, \phi) + k_{xy}(r = R_E, \theta, \phi) E_{DF,y}(t, r = R_E, \theta, \phi) \quad (5)$$

$$E_{CF,y}(t, r = R_E, \theta, \phi) = k_{yy}(r = R_E, \theta, \phi) E_{DF,y}(t, r = R_E, \theta, \phi) + k_{yx}(r = R_E, \theta, \phi) E_{DF,x}(t, r = R_E, \theta, \phi), \quad (6)$$

where t is time, r is radius, R_E is Earth radius, θ is colatitude, and ϕ is longitude. Juusola et al. (2025b) derived the proportionality coefficients k for Fennoscandia using the PGIEM2G (Polynomial Galerkin Integral Equation Modelling in ElectroMagnetic Geophysics) (Kruglyakov and Kuvshinov, 2018) induction code and the SMAP (Korja et al., 2002) 3-D ground conductivity model. Juusola et al. (2025b) provide the coefficients on a rectanglar grid with $0.03° \times 0.07°$ resolution in latitudinal and longitudinal directions. In order to estimate $\boldsymbol{E}_{CF}$ based on Eq. 5–6, the SECS method output $\boldsymbol{E}_{DF}$ was calculated for this grid. This grid was used for all GIC estimations based on IMAGE data (section 2.5).

As an example, in Figures 2 and 3 the modelled geoelectric field is compared to measurements. The figures show the south (E_θ, Fig. 2) and east (E_ϕ, Fig. 3) component of the geoelectric field at the Earth's surface on 26 June 1998 between 00:00:00 and 06:00:00 UT. The measured electric field at station B31 of the BEAR network is shown in blue, $E_{DF,\theta}$ estimated from BEAR (Fig. 2a and Fig. 3a), IMAGE (Fig. 2b and Fig. 3b), or SuperMAG (Fig. 2c and Fig. 3c) magnetometer measurements using the SECS method are shown in black, and the total modelled E_θ, estimated from $\boldsymbol{E}_{DF}$ using Eq. 5–6 is shown in red. The epoch of the maximum value for each curve is indicated by the labeled vertical line.

Direct comparison of measured and modelled geoelectric fields is often tricky. The electric charge distribution, which can include localized small-scale temporally varying structures driven by $\boldsymbol{E}_{DF}$, can contribute significantly to the observed values (e.g., Malone-Leigh et al., 2024). Such structures may be too small-scale to be described by the conductivity model (Korja et al., 2002) and thus are not included in the modelled total geoelectric field. Furthermore, the measured electric field data are often noisy (Lyon et al., 2025). In case of the BEAR data, there is also some ambiguity, due to unclear documentation, on the coordinate system of the data, i.e., whether the measured geoelectric field components are provided in geographic or local magnetic coordinates. Fortunately, the difference is small in Fennoscandia, and the data have been used successfully by, e.g., Viljanen et al. (2004) and Vanhamäki et al. (2013). Here, we have selected the station B31, for which the contribution to the electric field from charges is small according to the small difference between the black and red curves in Fig. 2 and 3. Despite the above-mentioned challenges, the measured and modelled geoelectric field values show reasonably good agreement. Visually, the best agreement is obtained using the dense BEAR magnetometer network, but the sparse IMAGE network provides very similar values. The agreement between B31 and SuperMAG modelling suffers somewhat from the lower cadence of the SuperMAG data even when B31 data are averaged to 1 min values.

2.4 Geoelectric field at Nagycenk, Hungary

In order to demonstrate the applicability of the estimated $\boldsymbol{E}_{DF}$ to areas outside of Fennoscandia, we need geoelectric field observations for comparison. Unlike most locations, 1-D modelling of the geoelectric field at Nagycenk (NCK; 47.63^o latitude and 16.72^o longitude) has been shown to reproduce the measured geoelectric field very well (Viljanen et al., 2012). Unlike 3-D modelling, 1-D modelling assumes that there are only conductivity variations in the vertical direction. We take advantage of

https://doi.org/10.5194/egusphere-2026-1110
Preprint. Discussion started: 13 March 2026

this property to produce a geoelectric field time series to be compared with $\boldsymbol{E}_{DF}$ estimated from SuperMAG data. The validity of the 1-D assumption does not necessarily mean that $\boldsymbol{E}_{CF}$ in the region is non-zero, but it means that the geoelectric field is not polarized. $\boldsymbol{E}_{CF}$ could still significantly affect the amplitude of the local geoelectric field when compared to $\boldsymbol{E}_{DF}$. As input to the 1-D modelling, a time series of the local magnetic field as well as a 1-D ground conductivity model are needed. We have extracted the magnetic field time series at NCK from the SuperMAG data set. The 1-D ground conductivity model consists of three layers: thicknesses 3 km and 57 km above an infinitely deep layer with resistivities (inverse of conductivity) of 5, 1000, and 10 Ωm, respectively.

2.5 GIC

We have used the method described by Viljanen et al. (2012) to estimate GIC in the Finnish benchmark power grid, which is the old Finnish 400 kV power grid used in 1978–1979. The benchmark power grid is described in detail by Viljanen et al. (2012). The present Finnish power grid is much more complex than the benchmark grid, with several tens of substations and many more power lines. The grounding resistances of the benchmark power grid were also much smaller than those of the present grid, allowing for significantly more intense GIC.

There is one significant difference between Viljanen et al. (2012) and our GIC calculation: when calculating the voltage V in the power line between substations j and i as a line integral of the horizontal geoelectric field $\boldsymbol{E}$

$$V_{ji} = \int_j^i \boldsymbol{E} \cdot \boldsymbol{dr}, \tag{7}$$

Viljanen et al. (2012) approximated $\boldsymbol{E}$ by a constant value, the mean of the field components parallel to the great circle at the end points j and i (see Figure A.1 in Viljanen et al. (2012) for an illustration). The shortest distance between two points on a sphere is along a great circle. A great circle is formed at the intersection of the spherical surface and a plane through the centre of the sphere. The assumption of constant $\boldsymbol{E}$ along a power line is not valid when the geoelectric field varies over distance scales similar or shorter than the power line lengths. Unlike the 1-D geoelectric field used by Viljanen et al. (2012), the 3-D geoelectric field we have used, and especially $\boldsymbol{E}_{CF}$, typically contains such structures. Thus, we have assumed that the geoelectric field remains constant only within each geoelectric field output grid cell, both for the triangular and rectangular grid. The grid cell edges and power lines were assumed to follow great circle arcs. Their intersection points were found by calculating the normalized cross product between the normal vectors of the two great circle planes, and by selecting the point located along the power line. This was done by comparing the sum of the two arc lengths, defined by the ends of the power line and the crossing point, to the length of the power line. This is illustrated in Figure 4. Any power lines that are not straight lines between two substations but have more complex structure can be described by adding virtual substations with infinite grounding resistances to locations where the power line changes direction.

As an example, Fig. 5 displays the GIC in the Finnish benchmark power grid on 26 June 1998 at 03:23:00 UT as driven by the total electric field estimated from BEAR magnetometer data using the SECS methods and Eq. 5–6. The total electric field in the grid area is shown by the orange arrows (only every 10th arrow is shown for clarity) and its intensity by the background

https://doi.org/10.5194/egusphere-2026-1110
Preprint. Discussion started: 13 March 2026

color. The powerlines are shown in black, and the black arrows with labels in the middle of each line indicate the amplitude and direction of current in each powerline. The labelled circles illustrate the amplitude of the current entering and leaving the power grid at each named substation. Blue color indicates current direction from ground to power grid and red color from power grid to ground. The size of the symbol at each substation is scaled according to the amplitude of GIC. Similarly, the relative thickness of the powerlines indicates the amplitude of current flow in the line.

2.6 Solar wind observations and SYM-H index

In order to discuss external drivers of GIC peaks, solar wind data from Magnetospheric Multiscale (MMS) mission (Burch et al., 2016), obtained via the MMS Science Data Center (Burch et al., 2025), were used. At the time of interest (10 May 2024 at 22:29 UT), MMS was located in the solar wind upstream of the Earth at Geocentric Solar Magnetospheric (GSM) coordinates $x = 12$, $y = -15$, and $z = -13$ $\mathrm{R_E}$. We obtained ion moments data from the Fast Plasma Investigation (FPI) (Pollock et al., 2016) instrument and calculated the solar wind dynamic pressure from the ion number density and ion bulk velocity. It should be noted that MMS ion moment data are not optimal for solar wind observations. However, we only use the data to time the arrival of solar wind structures previously identified in solar wind observatory data (e.g., Wallner et al., 2026). SYM-H index data (World Data Center for Geomagnetism, Kyoto et al., 2022), used to detect the arrival time of the solar wind dynamic pressure structure observed by MMS, were obtained via the World Data Center for Geomagnetism, Kyoto.

3 Results

Figure 6 provides an overview of the May 2024 geomagnetic storm. It shows latitude profiles of the east component of the ionospheric equivalent current density, derived from IMAGE data using the SECS method, at 23.9^o longitude between 10 May 2024 12:00 UT and 12 May 2024 12:00 UT. The selected longitude is located in the middle of the Finnish benchmark power grid. The storm onset occurred on 10 May 2024 at ∼17:08 UT (Lawrence et al., 2025). The two-hour time interval on 10 May 2024 between 21:30 and 23:30 UT, selected for further analysis, is indicated by the vertical dashed lines. The interval was centered around 22:29 UT, the time of the Karlshamn GIC incident (Rosenqvist et al., 2025; Wallner et al., 2026). The selected interval is characterised by the most southward extent of the westward electrojet (blue) during the storm. Poleward of the electrojet, the polar cap return current shows as eastward (red) equivalent current density. Solar wind observation and geomagnetic index context for the event have been shown previously by Wallner et al. (e.g., 2026).

3.1 GIC in the Finnish benchmark power grid

Table 1 shows the times of the largest GIC values at the substations of the Finnish benchmark power grid on 10 May 2024 between 21:30 and 23:30 UT. The values in the three columns of Table 1 have been calculated using the total geoelectric field and the DF component of the geoelectric field estimated from 10 s IMAGE observations and the DF component of the geoelectric field estimated from 1 min averaged IMAGE observation. We have used 1 min averaged IMAGE data instead

https://doi.org/10.5194/egusphere-2026-1110
Preprint. Discussion started: 13 March 2026

of 1 min SuperMAG data to keep the station configuration identical for both cadences. A different station configuration can produce slightly different results, and here we wish to isolate on the effect of the cadence.

The majority of the peak values calculated from 10 s $|\boldsymbol{E}|$ data and all peak values calculated from 10 s $|\boldsymbol{E}_{DF}|$ data occurred at 22:35:20–40 UT (blue color in Table 1), followed by 22:29:30–40 UT (red color in Table 1), coincident with the Karlshamn GIC incident. The largest value (426.1 A) of the entire interval, calculated from $\boldsymbol{E}$, took place at the southernmost substation, Inkoo, at 22:29:40 UT. As a reference, the most intense GIC measured in the Finnish power grid is 200 A (1 min average) at Rauma on 24 March 1991 (Viljanen and Pirjola, 1994). During the same geomagnetic storm, 175 A (10 s value) was measured at Pirttikoski. On 4 January 1979, 165 A (10 s value) was measured at Huutokoski. These values are in reasonable agreement with those in Table 1.

For the substations Hyvinkää, Olkiluoto, and Ulvila, the peak time calculated from $\boldsymbol{E}$ data occurred at 22:29:30–40 UT, but $\boldsymbol{E}_{DF}$ gave the peak between 22:35:20–40 UT. All these stations are located north of the region in southern Finland where relatively low ground conductivity tends to cause an intense electric field (Fig. 7d). Nurmijärvi is located at the same longitude as Hyvinkää and only 0.1^o in latitude south of it but showed opposite behavior in peak value timing: $\boldsymbol{E}$ gave the peak time at 22:34:20 UT and $\boldsymbol{E}_{DF}$ at 22:29:30 UT. However, the power grid geometry is different for the two substations: Hyvinkää is connected to Inkoo, Kangasala, and Nurmijärvi and Nurmijärvi is further connected to Loviisa. Most of the peak times calculated from 1 min data (last column) agree with their 10 s counterparts. The amplitudes are slightly weaker, as expected.

Figure 7a shows a time series of GIC at Inkoo substation, which had the largest peak value in Table 1. Inkoo is the single substation located at the southernmost tip of the Finnish benchmark power grid. This means that for north-south directed geoelectric field, GIC flowing across the power grid tend to funnel to Inkoo, resulting in relatively intense GIC flowing between the power grid and ground there. The different curves in Fig. 7a have been calculated using the total geoelectric field (red) and the DF component of the geoelectric field estimated from 10 s IMAGE observations (black) and using the DF component of the geoelectric field estimated from 1 min averaged IMAGE observations (blue). The peak times and amplitudes are indicated by vertical, labeled lines. At Inkoo, the direction of GIC is determined by $\boldsymbol{E}_{DF}$, but the total geoelectric field gives larger amplitudes. It should be noted that the amplitudes given by $\boldsymbol{E}$ can be overestimated because of the inaccuracy of the ground conductivity model (Marshalko et al., 2023). Despite giving slightly different peak epochs, the GIC calculated using $\boldsymbol{E}_{DF}$ from 10 s and from 1 min observations produce quite similar results, considering the occasionally considerable difference of 10 s and 1 min magnetic field time derivative amplitudes (cf. Juusola et al., 2023a, Figure 14). This is in agreement with previous results, according to which the relative difference is larger for $d\boldsymbol{B}/dt$ than for the geoelectric field (Pulkkinen et al., 2006; Grawe et al., 2018). The reason is that differentiation strongly amplifies the high-frequency content of the magnetic field variations, a significant portion of which is lost at 1 min sampling rate. The geoelectric field, on the other hand, is an inductive, conductivity-filtered response dominated by longer periods and therefore much less sensitive to the sampling rate.

Figure 7b shows a map of GIC in the Finnish benchmark power grid on 10 May 2024 at 22:29:40 UT in the same format as Fig. 5, calculated using $\boldsymbol{E}_{DF}$ from 10 s IMAGE observations. The structure of $\boldsymbol{E}_{DF}$ is too large-scale to show any significant variations across the power grid. The direction of $\boldsymbol{E}_{DF}$ is northward, thus driving GIC from the ground into the power grid at the southern substations and from the power grid into the ground at northern substations. The largest GIC occur at the edges

https://doi.org/10.5194/egusphere-2026-1110
Preprint. Discussion started: 13 March 2026

Table 1. Times and the most intense GIC values at the substations of the Finnish benchmark power grid on 10 May 2024 between 21:30 and 23:30 UT. The values in the three columns have been calculated using the total geoelectric field and the DF component of the geoelectric field estimated from 10 s IMAGE observations and the DF component of the geoelectric field estimated from 60 s averaged IMAGE observations. Times between 22:29:30 and 40 in 10 s data and the corresponding 22:30:00 UT in 1 min data are shown in red and times between 22:35:20 and 40 in 10 s data and the corresponding 22:36:00 UT in 1 min data are shown in blue. The largest GIC in each column is highlighted in **bold**.

Substation	IMAGE 10 s $\boldsymbol{E}$ UT (GIC [A])	IMAGE 10 s $\boldsymbol{E}_{DF}$ UT (GIC [A])	IMAGE 60 s $\boldsymbol{E}_{DF}$ UT (GIC [A])
Alajärvi	22:35:40 (-125.3)	22:35:40 (-36.4)	22:29:00 (23.3)
Alapitkä	22:35:30 (-31.1)	22:35:20 (58.0)	22:36:00 (42.2)
Huutokoski	22:35:30 (295.0)	22:35:30 (187.9)	22:36:00 (120.8)
Hyvinkää	22:29:40 (130.6)	22:35:40 (28.0)	22:29:00 (-15.9)
Inkoo	**22:29:40 (-426.1)**	22:29:30 (-134.9)	22:30:00 (-97.0)
Kangasala	22:34:20 (-21.2)	22:35:20 (-52.3)	22:36:00 (-40.8)
Koria	22:35:20 (25.8)	22:35:30 (84.3)	22:36:00 (47.3)
Letsi	22:35:30 (-208.8)	**22:35:30 (-218.2)**	**22:36:00 (-167.8)**
Lieto	22:35:20 (-112.7)	22:35:20 (-75.3)	22:30:00 (-45.2)
Loviisa	22:31:50 (273.7)	22:35:40 (134.0)	22:38:00 (-75.9)
Messaure	22:35:40 (-116.2)	22:35:30 (-157.7)	22:36:00 (-104.9)
Nurmijärvi	22:34:20 (-15.8)	22:29:30 (-36.1)	22:30:00 (-23.7)
Olkiluoto	22:29:30 (156.8)	22:35:20 (-170.6)	22:36:00 (-129.5)
Petäjäskoski	22:31:50 (-140.4)	22:29:30 (101.2)	22:41:00 (-67.5)
Pikkarala	22:40:50 (62.2)	22:35:20 (157.1)	22:36:00 (98.2)
Pirttikoski	22:35:20 (227.1)	22:35:20 (182.0)	22:36:00 (111.4)
Ulvila	22:29:30 (60.2)	22:35:30 (-35.6)	22:36:00 (-27.2)

of the network, as determined by the direction of $\boldsymbol{E}_{DF}$, i.e., at the southernmost and northernmost substations, whereas the substations in the middle of the network tend to have relatively weak GIC, in agreement with Viljanen et al. (2012).

Figure 7c and 7d are otherwise similar to Fig. 7b except that $\boldsymbol{E}_{CF}$ and $\boldsymbol{E}$ are used instead of $\boldsymbol{E}_{DF}$. The substation symbol sizes and power line widths in the three panels have been scaled to be comparable. $\boldsymbol{E}_{CF}$ modifies the large-scale GIC driven by $\boldsymbol{E}_{DF}$ by adding smaller-scale structure to it. The direction of the GIC across the network driven by $\boldsymbol{E}$ remains more or less the same as that driven by $\boldsymbol{E}_{DF}$. However, especially the region of low conductivity in southern Finland, characterised by high $\boldsymbol{E}_{CF}$ and $\boldsymbol{E}$, enhances the GIC flowing into the power grid at Inkoo, and out of the power grid at Olkiluoto and Hyvinkää, located north of the region of intense $\boldsymbol{E}$. In addition to the low conductivity, nearby conductivity gradients contribute to the intense $\boldsymbol{E}$ in southern Finland.

https://doi.org/10.5194/egusphere-2026-1110
Preprint. Discussion started: 13 March 2026

Figure 8a illustrates the GIC activity in the power grid during the two hour interval according to the sum of the absolute values of GIC at all substations in a format similar to Fig. 7a. Without the absolute value the sum would be zero as the amount of current entering and leaving the network must be equal. The GIC sums calculated using 10 s $\boldsymbol{E}$ or $\boldsymbol{E}_{DF}$ follow each other relatively well, although occasionally the amplitude given by $\boldsymbol{E}_{DF}$ is weaker than that given by $\boldsymbol{E}$. For example, this is the case at 22:29:30–40 UT, when $\boldsymbol{E}_{DF}$ was northward and the conductivity structure in southern Finland strongly amplified the GIC in this region. On the other hand, at 22:35:20–40 UT when $\boldsymbol{E}_{DF}$ was mainly westward (not shown), the GIC sums given by 10 s $\boldsymbol{E}$ or $\boldsymbol{E}_{DF}$ are almost equal. The GIC sum calculated from 1 min $\boldsymbol{E}_{DF}$ gives a relatively good indication of enhanced GIC levels.

The effect of $\boldsymbol{E}_{DF}$ direction on the intensification of the GIC by $\boldsymbol{E}_{CF}$ is illustrated in Fig. 8c, which shows the relative GIC sum calculated using $\boldsymbol{E}$ and $\boldsymbol{E}_{DF}$ as a function of average $\boldsymbol{E}_{DF}$ direction in the network area. For southward (0^o) and northward $\boldsymbol{E}_{DF}$ ($\pm 180^o$), the GIC sum calculated using $\boldsymbol{E}$ is about twice as large as as that calculated using $\boldsymbol{E}_{DF}$, while for eastward (90^o) and westward (-90^o) $\boldsymbol{E}_{DF}$, the sums are almost equal. The main reason for this is the area in southern Finland, where the geoelectric field is strongly amplified for northward and southward $\boldsymbol{E}_{DF}$ (cf. Juusola et al., 2025b, Figure 15). This is also illustrated by Fig. 8b and 8d, which are otherwise the same as Fig. 8a and 8c, except that the power grid has been shifted 1^o northward in latitude, placing Inkoo well north of the critical area (cf. Fig. 7d). Now the GIC sums calculated using $\boldsymbol{E}_{DF}$ and $\boldsymbol{E}$ are almost equal and the direction of $\boldsymbol{E}_{DF}$ has much less effect on the relative GIC sum.

3.2 Norwegian coast

As we have seen, even a relatively small area where the geoelectric field is strongly amplified by $\boldsymbol{E}_{CF}$ can significantly affect GIC at the nearby substations. Even stronger geoelectric field amplification than in southern Finland occurs at the Norwegian coast (cf. Juusola et al., 2025b, Figure 15). We will examine the effect on GIC by shifting the Finnish grid such that Olkiluoto substation is moved to 64.5^o latitude and 11.5^o longitude, keeping the power grid geometry intact. As illustrated by Fig. 9, this places Olkiluoto on the coast in the region of strongly enhanced geoelectric field such that the line between Olkiluoto and Lieto bridges the coastal enhancement and ends just outside of it. Fig. 9 illustrates the strong enhancement of the GIC calculated using $\boldsymbol{E}$ instead of $\boldsymbol{E}_{DF}$. The strongest $\boldsymbol{E}$ occurs when $\boldsymbol{E}_{DF}$ is directed perpendicular to the coast (Fig. 9b), as expected (cf. Juusola et al., 2025b, Figure 15). This is further illustrated by Figure 10, in a format similar to Fig. 8b and 8d. For the Norwegian coast, the GIC sum calculated using $\boldsymbol{E}$ can be three times larger than that calculated using $\boldsymbol{E}_{DF}$, when $\boldsymbol{E}_{DF}$ is directed perpedicular to the coastline ($\boldsymbol{E}_{DF}$ direction angles -120^o and 60^o). For $\boldsymbol{E}_{DF}$ directed parallel to the coast line (-30^o and 150^o), the GIC sums are nearly equal.

As mentioned in the Introduction, a transformer in mid-Norway, close to the location of the shifted Olkiluoto station, tripped during the May 2024 geomagnetic storm. However, this occurred much later than the time interval studied here, on the morning of 11 May 2024, between 4 and 5 UT. It is likely that, since the Norwegian power grid in this region is purely following the coast, the geoelectric field component along the transmission line was not sufficiently intense to create GIC strong enough to produce any effects during the time interval studied here as opposed to the morning of 11 May.

https://doi.org/10.5194/egusphere-2026-1110
Preprint. Discussion started: 13 March 2026

Thus, we can conclude that, in the absence of ground conductivity information and higher-cadence magnetic field observations, 1 min magnetic field data alone can provide a reasonable proxy for GIC activity in a power grid. However, some substations are strongly affected by local ground conductivity gradient structures and the GIC amplitude at such substations may be poorly described by $\boldsymbol{E}_{DF}$.

3.3 Drivers of geoelectric field peaks in Northern Europe

Figure 11 shows the ionospheric equivalent current density ($\boldsymbol{J}_{eq}$, Fig. 11a), its time derivative (Fig. 11b), corresponding external $\boldsymbol{E}_{DF}$ on the ground (Fig. 11c), telluric current density (Fig. 11d), its time derivative (Fig. 11e), corresponding internal $\boldsymbol{E}_{DF}$ on the ground (Fig. 11f), and total $\boldsymbol{E}_{DF}$ on the ground (Fig. 11g) at the time of the Inkoo GIC peak on 10 May 2024 at 22:29:40 UT. The maps have been derived from 10 s IMAGE magnetometer observations, indicated by red dots on the map. In areas where the magnetometer density is small, the equivalent current only gives a rough indication of the large-scale currents. The GIC peak time was characterised by an intense (maximum value > 2000 Akm^{-1}) westward electrojet over southern Finland and Sweden. This is an exceptionally southern location for the electrojet, which under nominal conditions is generally located poleward of about 63^o N (Ritter et al., 2004).

There is a southward undulation in the electrojet between Sweden and Finland, and the external $\boldsymbol{E}_{DF}$ (Fig. 11c) is directed northward, opposing the deepening of the undulation (Fig. 11b). The telluric equivalent current density (Fig. 11d) is mainly directed opposite to the ionospheric equivalent current density but the internal part of $\boldsymbol{E}_{DF}$ (Fig. 11f) associated with its temporal variations (Fig. 11e) is clearly weaker than the external $\boldsymbol{E}_{DF}$. Thus, the total $\boldsymbol{E}_{DF}$ (Fig. 11g) is dominated by the external component. The associated ionospheric equivalent current dynamics are further discussed by Wallner et al. (2026).

Figure 12 shows similar plots for 10 May 2024 at 22:35:30 UT, which was the time when the largest GIC peak was observed in the power grid shifted to the Norwegian coast. The equivalent current (Fig. 12a) amplitude is somewhat larger than in Fig. 11, but the distribution remains quite similar. Now the external $\boldsymbol{E}_{DF}$ (Fig. 12c) opposes the general strengthening of the equivalent current density (Fig. 12b). The total $\boldsymbol{E}_{DF}$ (Fig. 12g) is again only slightly modified by the internal $\boldsymbol{E}_{DF}$ (Fig. 12f).

3.4 Drivers of geoelectric field peaks in Central Europe

Figure 13 compares the external part of $\boldsymbol{E}_{DF}$ calculated from 1 min SuperMAG data to the modelled 1-D geoelectric field $\boldsymbol{E}_{1D}$ at Nagycenk (NCK), Hungary, on 10 May 2024 at 15:00:00–23:59:00 UT. This interval covers the beginning of the storm as well as the two-hour period around the Karlshamn incident. We have used $\boldsymbol{E}_{DF,ext}$ instead of $\boldsymbol{E}_{DF}$, because in this region the magnetometer density is not dense enough to properly describe the internal part of $\boldsymbol{E}_{DF}$, which typically contains smaller-scale structures than the external part of $\boldsymbol{E}_{DF}$, especially south of the auroral region (see the location of NCK with respect to the auroral electrojets in Figure 14a and d).

The validity of the 1-D assumption at NCK (Viljanen et al., 2012) indicates that the geoelectric field is not polarized. However, the relatively high conductivity (section 2.4) still markedly weakens the geoelectric field amplitude compared to $\boldsymbol{E}_{DF}$, and especially to $\boldsymbol{E}_{DF,ext}$, because $\boldsymbol{E}_{DF,int}$ is typically oppositely directed to $\boldsymbol{E}_{DF,ext}$, resulting in a total $\boldsymbol{E}_{DF}$ that is much weaker in amplitude than either $\boldsymbol{E}_{DF,ext}$ or $\boldsymbol{E}_{DF,int}$ (Juusola et al., 2025b). To compensate for this, we have

https://doi.org/10.5194/egusphere-2026-1110
Preprint. Discussion started: 13 March 2026

determined the k coefficients of Eq. 5–6 by a least squares fit of $\boldsymbol{E}_{DF,ext}$ to $\boldsymbol{E}_{1D}$ from 10 May 2024 12:00:00 UT to 12 May 2024 11:59:00 UT. The resulting values are: $k_{xx} = -0.953$, $k_{xy} = 0.007$, $k_{yy} = -0.963$, and $k_{yx} = 0.016$. Fig. 13a–b show a reasonable agreement between $\boldsymbol{E}_{DF,ext}$ and $\boldsymbol{E}_{1D}$ time development. Because $\boldsymbol{E}_{DF,ext}$ amplitudes are much larger than those of $\boldsymbol{E}_{1D}$ or $\boldsymbol{E}$ estimated from $\boldsymbol{E}_{DF,ext}$ using the above coefficients, we have scaled $\boldsymbol{E}_{DF,ext}$ in Fig. 13 such that the median of $|\boldsymbol{E}_{DF,ext}|$ becomes equal to the median of $|\boldsymbol{E}_{1D}|$ for the two day interval.

The most pronounced features in Fig. 13 are the peaks at the storm sudden commencement at 17:07:00 UT and the bipolar E_θ variation (Fig. 13a) with the maximum $|\boldsymbol{E}_{1D}|$ (Fig. 13c) at 22:36:00 UT. The storm sudden commencement peak due to an interplanetary shock arrival was characterized by a strong sudden increase of the magnetopause and ring currents (Piersanti et al., 2025). Global ionospheric current density, its time derivative, and the external ground DF geoelectric field on 10 May 2024 at 17:07:00, derived from global 1 min SuperMAG data are shown in Figure 14a–c. The ionospheric equivalent current pattern (Fig. 14a) is undergoing a transition from pre-shock to post-shock state and its time derivative (Fig. 14b) illustrates the increasing magnetopause current (eastward pointing arrows) at lower latitudes and the appearance of a double vortex pattern at higher latitudes over North America. The associated external DF electric field on the ground (Fig. 14c) naturally opposes these changes, producing the intense peak of mainly westward electric field in Europe.

The total geoelectric field estimated across Britain reached its storm maximum value at 22:36:00 UT (Lawrence et al., 2025), simultaneously with the NCK $|\boldsymbol{E}_{1D}|$ peak. Such large-scale dynamics indicate a solar wind driver (Pulkkinen et al., 2003c) as well. In order to examine this further, Figure 15 shows solar wind dynamic pressure observed by the MMS1 satellite, located in the solar wind upstream of the Earth. The peak around 22:35 UT has been previously identified from Wind spacecraft ion density observations by Wallner et al. (2026). The SYM-H index, according to the right hand side axis, is also shown in the panel. The MMS1 data have been delayed by 197 s to match the peak times of the dynamic pressure and SYM-H. The epoch 22:36:00 UT is indicated with a vertical line. Clearly, it was part of the geoelectric field response to a transient solar wind dynamic pressure increase.

The equivalent current distribution in Fig. 14d shows the two-cell convection pattern with the eastward electrojet in the dusk sector, the westward electrojet in the dawn sector, and antisunward return current across the polar cap. More detail and larger amplitudes can be discerned in areas more densely covered by magnetometers (red dots) whereas sparsely covered areas only show coarse large-scale features. Compared to Fig. 1c, which took place under more moderate geomagnetic activity, the electrojets in Fig. 14a have expanded to significantly lower latitudes. The external $\boldsymbol{E}_{DF}$ (Fig. 14f) opposes the changes in the ionospheric (Fig. 14e) equivalent currents. These changes include a weakening magnetopause current, represented as large-scale westward ionospheric $d\boldsymbol{J}_{eq}/dt$ and eastward external $\boldsymbol{E}_{DF}$ on the dayside, as a response to weakening solar wind dynamic pressure (Fig. 15). The peak GIC at the benchmark power grid shifted to the Norwegian coast also took place during the same dynamic pressure weakening (Fig. 12).

https://doi.org/10.5194/egusphere-2026-1110
Preprint. Discussion started: 13 March 2026

4 Discussion

4.1 Recipe for intense GIC

We have examined the contributions from $\boldsymbol{E}_{DF}$ and $\boldsymbol{E}_{CF}$ to GIC, using the Finnish benchmark power grid as an example. $\boldsymbol{E}_{DF}$, which is associated with $d\boldsymbol{B}/dt$ and can thus be obtained from ground-based magnetometer network observations alone, tends to be spatially relatively smooth. Deriving $\boldsymbol{E}_{CF}$ requires additional information on the ground conductivity distribution. Compared to $\boldsymbol{E}_{DF}$, $\boldsymbol{E}_{CF}$ tends to contain structures that are much smaller in spatial scale, but can be much more intense. The reason is that the external currents that create the external $\boldsymbol{E}_{DF}$ are located at least 90 km above the observer and, consequently, any small-scale structures are attenuated on the ground (Untiedt and Baumjohann, 1993). The telluric currents that create the internal part of $\boldsymbol{E}_{DF}$ may flow very close to the observer, but nonetheless they are more smoothly spread out in the conducting ground than the charges that are strongly concentrated at conductivity gradients and thus create the highly structured $\boldsymbol{E}_{CF}$. We found that while $\boldsymbol{E}_{DF}$ determines the overall direction and level of GIC activity in the power grid, $\boldsymbol{E}_{CF}$ can produce localized enhancements that can significantly modify the GIC amplitudes at nearby substations for certain directions of the $\boldsymbol{E}_{DF}$.

$\boldsymbol{E}_{DF}$ comprises an external part due to time-varying ionospheric and magnetospheric currents and an internal part due to time-varying telluric currents. These two contributions tend to be oppositely oriented with comparable amplitudes, typically resulting in a small residual $\boldsymbol{E}_{DF}$ that is much weaker in amplitude than either the external or internal part alone (Juusola et al., 2025b). In our examples, GIC peaks occurred at times when the internal and external part were "out of phase", i.e., one component was strongly suppressed compared to the other, resulting in a strong peak in the total $\boldsymbol{E}_{DF}$. Intense total $\boldsymbol{E}$ further required that $\boldsymbol{E}_{DF}$ was optimally directed with respect to any potentially intensifying conductivity gradient structures in the area, and intense GIC that the intense $\boldsymbol{E}$ was optimally directed with respect to the power grid geometry, i.e., an intense field along the power lines. The significant role of ground conductivity is in line with the important observation of Love et al. (2022) that latitude-dependent organization of geoelectric hazards by auroral-zone electrojet currents, although detectable, is much weaker than geographic organization due to surface impedance.

4.2 Usefulness and weaknesses of global $\boldsymbol{J}_{eq}$ and $\boldsymbol{E}_{DF}$ maps

The SECS method has been widely used in the past to determine regional ionospheric equivalent current distributions from regional ground-based magnetometer network observations (e.g., Pulkkinen et al., 2003a; Weygand et al., 2011). The method has the advantage that the spatial resolution of the solution can be adapted to the local observation density (e.g., Weygand et al., 2011), although this feature has not been very extensively exploited in the past. Globally, the magnetometer distribution is highly non-uniform. Optimal analysis of such data requires that in areas where the magnetometer coverage is dense, the solution can also contain smaller scale structures and in areas where the magnetometer coverage is sparse, only large-scale structures can be modelled. We have demonstrated how using the SECS method with a global triangular grid adapted to magnetometer density allows estimating the global distribution of $\boldsymbol{J}_{eq}$ and $\boldsymbol{E}_{DF}$ from SuperMAG magnetometer data. Previous applications of the SECS method, including the global $\boldsymbol{J}_{eq}$ maps derived by Huttunen et al. (2002) for one event, have typically used rectangular grids.

https://doi.org/10.5194/egusphere-2026-1110
Preprint. Discussion started: 13 March 2026

At high latitudes, ionospheric equivalent current density at 90 km altitude can be interpreted as the DF part of the horizontal ionospheric current density. A general approach for deriving global maps of $\boldsymbol{J}_{eq}$ has been to obtain a proxy by simply rotating ground-based horizontal magnetic field variations 90^o (e.g., Gjeloev, 2025). Benkevitch et al. (2006) has shown that there is a reasonable agreement in direction (within 45 degrees) between such "magnetic equivalent convection" and SuperDARN convection vectors. This was further elaborated by Weygand et al. (2011) using the SECS technique. The rotation of the magnetic field vectors, however, does not separate the internal and external contributions and retains the unit of magnetic field instead of current density. Combining $\boldsymbol{J}_{DF}$ with $\boldsymbol{J}_{CF}$ derived, for example, from Active Magnetosphere and Planetary Electrodynamics Response Experiment (AMPERE; Anderson et al., 2002) field-aligned current data products, yields the total ionospheric horizontal current density. Including global Super Dual Auroral Radar Network (SuperDARN; Chisham et al., 2007) potential electric field maps allows, for example, global estimates of Joule heating to be calculated (Green et al., 2007). An alternative approach would be to combine the global ionospheric $\boldsymbol{J}_{DF}$ and $\boldsymbol{E}_{DF}$ with global conductance maps, estimated from satellite images or empirical models, and solving for the complete set of ionospheric electrodynamical parameters (Juusola et al., 2025c). The DF ionospheric horizontal current density can also be valuable for placing other local observations, such as auroral emission or scintillation, into context within the large-scale auroral electrojets (e.g., Jacobsen et al., 2025).

We have shown that the SECS method can produce an $\boldsymbol{E}_{DF}$ time series that has a reasonably good agreement with an observed $\boldsymbol{E}$, both in direction and amplitude. In areas where the magnetometer density is sparse, however, any structures of $\boldsymbol{E}_{DF}$ smaller than the magnetometer network spacing will not be properly described due to the long range of $\boldsymbol{E}_{DF}$ compared to $d\boldsymbol{B}/dt$ (Juusola et al., 2025b). In central Europe, the magnetometer density is much lower than in northern Europe. Central Europe is typically located in the subauroral region, where the external $\boldsymbol{E}_{DF}$ is expected to be smoother than in the auroral region due to the generally greater distance to the driving current systems. A sparse magnetometer network will not be able to resolve such features in detail, introducing error to the resulting $\boldsymbol{E}_{DF}$. This problem can be partially mitigated by examining the external part of the $\boldsymbol{E}_{DF}$ alone, as we have demonstrated in section 3.4. A strength of our method is that in addition to the geoelectric field, it also gives the equivalent currents and thus provides information on the external driver, as we have demonstarted in this study.

As we have shown, $\boldsymbol{E}_{CF}$ can have a very strong, although typically relatively localized, effect on GIC. The localized nature of $\boldsymbol{E}$ enhancements due to $\boldsymbol{E}_{CF}$ is also discussed by Viljanen et al. (2026). While the conductivity model available for central Europe (Alekseev et al., 2015) is relatively coarse, combined with a recent global 3-D conductivity model of the world ocean and marine sediments (Grayver, 2021) would still allow including the coast effect due to ocean-land conductivity contrasts, as was done in Portugal (Ribeiro et al., 2021) before a field measurement campaign was carried out to complete a 50×50 km grid of MT soundings over the whole territory (Ribeiro et al., 2023).

5 Conclusions

We have applied spherical elementary current systems on a triangular grid adapted to local magnetometer density to calculate regional and global ionospheric and telluric equivalent currents and geoelectric fields from 10 s IMAGE and 1 min SuperMAG

https://doi.org/10.5194/egusphere-2026-1110
Preprint. Discussion started: 13 March 2026

magnetometer observations during the May 2024 geomagnetic superstorm. The roles of different geoelectric field contributions in driving GIC were assessed by calculating the resulting GIC in the Finnish benchmark power grid. The most intense GIC peak in the Finnish benchmark power grid during a two-hour interval of the storms coincided with a recorded GIC incident in Karlshamn, Sweden (Rosenqvist et al., 2025). Our conclusions are the following:

1. In the absence of ground conductivity information, the divergence-free geoelectric field ($\boldsymbol{E}_{DF}$) estimated from variation magnetic field observations alone can provide a reasonable proxy for GIC activity in a power grid.
2. In the absence of higher-cadence magnetic field observations, 1 min data provides a reasonable estimate for $\boldsymbol{E}_{DF}$, in agreement with Pulkkinen et al. (2006) and Grawe et al. (2018).
3. Polarization of the geoelectric field due to lateral variations in ground conductivity can produce intense GIC (e.g., three-fold compared to $\boldsymbol{E}_{DF}$) at substations connected to transmission lines traversing regions of enhanced geoelectric field. GIC at such substations may be poorly described by $\boldsymbol{E}_{DF}$ alone.
4. Adopting the adaptable triangular grid for the SECS method provides a robust tool for optimal analysis of ground-based magnetometer data, scalabale to both regional and global magnetometer distributions.

Because $\boldsymbol{E}_{DF}$ is much smoother spatially than $\boldsymbol{E}$, and fast to calculate, it could also be useful as a tool for assessing long-term GIC risks. Whereas $\boldsymbol{E}$ can vary by orders of magnitude at a given time within the area covered by a power grid, for example, $\boldsymbol{E}_{DF}$ can remain more or less constant, allowing more straightforward comparison of the effective geoelectric field at different times.

Code and data availability. IMAGE (Juusola et al., 2025a), SuperMAG (Gjeloev, 2025), MMS (Burch et al., 2025) data are freely available. The SYM-H index used in this paper was provided by the WDC for Geomagnetism, Kyoto (https://wdc.kugi.kyoto-u.ac.jp/wdc/Sec3.html). The code for the SECS method is available as a supplement to Vanhamäki and Juusola (2020). A python code for creating a triangular grid is available at Zenodo (Honkonen, 2025). BEAR data are available via the EPOS portal https://www.ics-c.epos-eu.org/.

Appendix A: Triangular grid

A1 Basic grid

We use the following procedure for creating the triangular grid: We start with a regular icosahedron with edge length of 1, consisting of 20 triangular cells and represented by 12 vertices at the following Cartesian coordinates (e.g., Steeb et al., 2012): $(0, \pm\phi^{-1}, \pm 1)$, $(\pm\phi^{-1}, \pm 1, 0)$, $(\pm 1, 0, \pm\phi^{-1})$, where $\phi = (1+\sqrt{5})/2$ is the golden ratio. We then rotate the grid by the angle $tan^{-1} - \phi$ about the y axis with the resulting vertex coordinates listed in Table A1. A triangular cell is refined by replacing it with four smaller cells with the new vertices evenly subdiving the original cell's edges and with same radius as other vertices.

https://doi.org/10.5194/egusphere-2026-1110
Preprint. Discussion started: 13 March 2026

Table A1. Cartesian coordinates of the initial triangular grid's vertices.

x	y	z
0.0000	0.0000	1.1756
0.6180	0.8507	0.5257
-0.6180	0.8507	0.5257
1.0000	-0.3249	0.5257
-1.0000	-0.3249	0.5257
0.0000	-1.0515	0.5257
0.0000	1.0515	-0.5257
1.0000	0.3249	-0.5257
-1.0000	0.3249	-0.5257
0.6180	-0.8507	-0.5257
-0.6180	-0.8507	-0.5257
0.0000	0.0000	-1.1756

A2 Adaptation to magnetometer density

A triangular grid adapted to the magnetometer density was used for the DF SECS poles. The grid was constructed as follows: First, an icosahedron was created (Figure A1a), as described in Appendix A1. Next, the number of magnetometers within each triangle was calculated. Whether a magnetometer was inside a given triangular cell was determined by comparing the spherical triangle area of the cell to the sum of the three triangle areas defined by the three vertices of the triangle cell and the magnetometer location. As long as there was more than one magnetometer inside a triangle, that triangle was split into four triangles (Fig. A1b–c). Finally, all triangles with a magnetometer inside them were split once more (Fig. A1e, Fig. A2a) to provide enough parameters to fit the observed magnetic field components. Without this last step, the matrix inversion required to determine the SECS amplitudes did not produce sensible results.

SECS poles were placed in the middle of each triangle at 1 m depth and at 90 km altitude. SuperMAG had a few magnetometers located very close to each other, which would have produced very small grid cells. With very small grid cells, even a small inconsistency in the neighboring magnetic field observations can produce large current densities. To avoid this, any SuperMAG stations within 50 km of another station were first removed. For visualizing the output, a uniform grid was used (Fig. A1f). For the regional IMAGE and BEAR results, a denser output grid (Fig. A2b) was used and only the region covered by observations was displayed. The output grid spacings were selected according to visual clarity when plotted on maps. Naturally, in areas where the output grid is sparser than the SECS grid, structures smaller that the output grid will be discarded. In areas where the output grid is denser than the SECS grid, it is important to bear in mind that structures smaller than the SECS grid spacing will not be described. It would also be possible to use the SECS grid as output grid, but such a grid is generally not visually optimal, espcially for global maps with large variations in grid density.

https://doi.org/10.5194/egusphere-2026-1110
Preprint. Discussion started: 13 March 2026

Author contributions. LJ implemented the method and prepared the manuscript. AV provided expert advice on geomagnetic induction and GIC. IH implemented the code for creating a basic triangular grid (provided as a supplement) and prepared Appendix A1. MGJ provided information on the Norwegian power grid and local GIC events. All co-authors participated in writing the manuscript.

Competing interests. The authors declare that they have no conflict of interest.

Acknowledgements. We thank the institutes who maintain the IMAGE Magnetometer Array: Tromsø Geophysical Observatory of UiT the Arctic University of Norway (Norway), Finnish Meteorological Institute (Finland), Institute of Geophysics Polish Academy of Sciences (Poland), GFZ German Research Centre for Geosciences (Germany), Geological Survey of Sweden (Sweden), Swedish Institute of Space Physics (Sweden), Sodankylä Geophysical Observatory of the University of Oulu (Finland), DTU Technical University of Denmark (Denmark), and Science Institute of the University of Iceland (Iceland). The provisioning of data from AAL, GOT, HAS, NRA, VXJ, FKP, ROE, BFE, BOR, HOV, SCO, KUL, and NAQ is supported by the ESA contracts number 4000128139/19/D/CT as well as 4000138064/22/D/KS.

For the ground SuperMAG magnetometer data we gratefully acknowledge: INTERMAGNET; USGS Geomagnetism Program; CARISMA, PI Ian Mann; CANMOS, Geomagnetism Unit of the Geological Survey of Canada; The S-RAMP Database, PI K. Yumoto and Dr. K. Shiokawa; The SPIDR database; AARI, PI Oleg Troshichev; The MACCS program, PI M. Engebretson; GIMA; MEASURE, UCLA IGPP and Florida Institute of Technology; SAMBA, PI Eftyhia Zesta; 210 Chain, PI K. Yumoto; SAMNET, PI Farideh Honary; IMAGE, PI Liisa Juusola; Finnish Meteorological Institute, PI Liisa Juusola; Sodankylä Geophysical Observatory, PI Tero Raita; UiT the Arctic University of Norway, Tromsø Geophysical Observatory, PI Magnar G. Johnsen; GFZ German Research Centre For Geosciences, PI Jürgen Matzka; Institute of Geophysics, Polish Academy of Sciences, PI Anne Neska and Jan Reda; Polar Geophysical Institute, PI Alexander Yahnin and Yarolav Sakharov; Geological Survey of Sweden, PI Gerhard Schwarz; Swedish Institute of Space Physics, PI Masatoshi Yamauchi; AUTUMN, PI Martin Connors; DTU Space, Thom Edwards and PI Anna Willer; South Pole and McMurdo Magnetometer, PI's Louis J. Lanzarotti and Alan T. Weatherwax; ICESTAR; RAPIDMAG; British Artarctic Survey; McMac, PI Dr. Peter Chi; BGS, PI Dr. Susan Macmillan; Pushkov Institute of Terrestrial Magnetism, Ionosphere and Radio Wave Propagation (IZMIRAN); MFGI, PI B. Heilig; University of L'Aquila, PI M. Vellante; BCMT, V. Lesur and A. Chambodut; Data obtained in cooperation with Geoscience Australia, PI Andrew Lewis; PENGUIn, co-PIs Bob Clauer, Michael Hartinger, and Zhonghua Xu; MagStar, PI Jennifer Gannon; LISN PI Cesar Valladares; Geophysical and Astronomical Observatory of the University of Coimbra, PI Paulo Ribeiro; Leibniz Institute of Atmospheric Physics, PI Jorge Chau; SuperMAG, PI Rafael Mesquita; Data obtained in cooperation with the Australian Bureau of Meteorology, PI Richard Marshall. LJ and AV acknowledge funding from the Research Council of Finland (grant 374099-SpaceResilience).

https://doi.org/10.5194/egusphere-2026-1110
Preprint. Discussion started: 13 March 2026

References

Alekseev, D., Kuvshinov, A., and Palshin, N.: Compilation of 3D global conductivity model of the Earth for space weather applications, Earth Planets Space, 67, https://doi.org/10.1186/s40623-015-0272-5, 2015.

Amm, O.: Ionospheric elementary current systems in spherical coordinates and their application, J. Geomagn. Geoelectr., 49, 947–955, https://doi.org/10.5636/jgg.49.947, 1997.

Amm, O. and Viljanen, A.: Ionospheric disturbance magnetic field continuation from the ground to ionosphere using spherical elementary current systems, Earth Planets Space, 51, 431–440, https://doi.org/https://dx.doi.org/10.1186/BF03352247, 1999.

Anderson, B. J., Takahashi, K., Kamei, T., Waters, C. L., and Toth, B. A.: Birkeland current system key parameters derived from Iridium observations: Method and initial validation results, J. Geophys. Res., 107(A6), https://doi.org/10.1029/2001JA000080, 2002.

Benkevitch, L. V., Koustov, A. V., Liang, J., and Watermann, J. F.: Comparison of the magnetic equivalent convection direction and ionospheric convection observed by the SuperDARN radars, Ann. Geophys., 24, 2981–2990, https://doi.org/10.5194/angeo-24-2981-2006, 2006.

Boteler, D. H.: A new versatile method for modelling geomagnetic induction in pipelines, Geophysical Journal International, 193, 98–109, https://doi.org/10.1093/gji/ggs113, 2013.

Burch, J., Fowler, G., and Le, G.: MMS science data [data set], https://lasp.colorado.edu/mms/sdc/public/, last access: February 26, 2026, 2025.

Burch, J. L., Moore, T. E., Torbert, R. B., and Giles, B. L.: Magnetospheric Multiscale Overview and Science Objectives, Space Sci. Rev., 199, 5–21, https://doi.org/10.1007/s11214-015-0164-9, 2016.

Chisham, G., Lester, M., Milan, S. E., Freeman, M. P., Bristow, W. A., Grocott, A., McWilliams, K. A., Ruohoniemi, J. M., Yeoman, T. K., Dyson, P. L., Greenwald, R. A., Kikuchi, T., Pinnock, M., Rash, J. P. S., Sato, N., Sofko, G. J., Villain, J.-P., and Walker, A. D. M.: A decade of the Super Dual Auroral Radar Network (SuperDARN): scientific achievements, new techniques and future directions, Surv. Geophys., 28, 33–109, https://doi.org/10.1007/s10712-007-9017-8, 2007.

Cordell, D., Unsworth, M. J., Lee, B., Hanneson, C., Milling, D. K., and Mann, I. R.: Estimating the geoelectric field and electric power transmission line voltage during a geomagnetic storm in Alberta, Canada using measured magnetotelluric impedance data: The influence of three-dimensional electrical structures in the lithosphere, Space Weather, 19, e2021SW002 803, https://doi.org/10.1029/2021SW002803, 2021.

Cordell, D., Mann, I. A., Dimitrakoudis, S., Parry, H., and Unsworth, M. J.: Long-term peak geoelectric field behavior for space weather hazard assessment in Alberta, Canada using geomagnetic and magnetotelluric measurements, Space Weather, 23, e2024SW004 305, https://doi.org/10.1029/2024SW004305, 2025.

Fu, W. D., Fu, H. S., Zhang, W. Z., Yu, Y., and Cao, J. B.: Compression of Earth's magnetopause down to 5 RE during the superstorm on 10 May 2024, Geophysical Research Letters, 52, e2024GL114 040, https://doi.org/10.1029/2024GL114040, 2025.

Gjeloev, J. W.: SuperMAG [data set], https://supermag.jhuapl.edu/, last access: February 26, 2026, 2025.

Gjerloev, J. W.: The SuperMAG data processing technique, J. Geophys. Res., 117, https://doi.org/10.1029/2012JA017683, 2012.

Gonzalez-Esparza, J. A., Sanchez-Garcia, E., Sergeeva, M., Corona-Romero, P., Gonzalez-Mendez, L. X., Valdes-Galicia, J. F., Aguilar-Rodriguez, E., Rodriguez-Martinez, M., Ramirez-Pacheco, C., Castellanos, C. I., Pazos, M., Mendoza, B., Gatica-Acevedo, V. J., Melgarejo-Morales, A., Caraballo, R., Andrade-Mascote, E., Villanueva-Hernandez, P., Bonifaz-Alfonzo, R., Sierra, P., Romero-Hernandez, E., Peralta-Mendoza, I., Perez-Tijerina, E., Mejia-Ambriz, J. C., Guerrero-Peña, C., Caccavari, A., Cifuentes-Nava, G., and

https://doi.org/10.5194/egusphere-2026-1110
Preprint. Discussion started: 13 March 2026

Hernandez-Quintero, E.: The mother's day geomagnetic storm on 10 May 2024: Aurora observations and low latitude space weather effects in Mexico, Space Weather, 22, e2024SW004 111, https://doi.org/10.1029/2024SW004111, 2024.

Grawe, M. A., Makela, J. J., Butala, M. D., and Kamalabadi, F.: The impact of magnetic field temporal sampling on modeled surface electric fields, Space Weather, 16, 1721–1739, https://doi.org/10.1029/2018SW001896, 2018.

Grayver, A. V.: Global 3-D electrical conductivity model of the world ocean and marine sediments, Geochemistry, Geophysics, Geosystems, 22, e2021GC009 950, https://doi.org/10.1029/2021GC009950, 2021.

Green, D. L., Waters, C. L., Korth, H., Anderson, B. J., Ridley, A. J., and Barnes, R. J.: Technique: Large-scale ionospheric conductance estimated from combined satellite and ground-based electromagnetic data, J. Geophys. Res., 112, A05303, https://doi.org/10.1029/2006JA012069, 2007.

Haines, G. V. and Torta, J. M.: Determination of equivalent current sources from spherical cap harmonic models of geomagnetic field variations, Geophysical Journal International, 118, 3, 499–514, https://doi.org/10.1111/j.1365-246X.1994.tb03981.x, 1994.

Honkonen, I.: Adaptable triangular grid on sphere (Version 1) [code], Zenodo, https://doi.org/10.5281/zenodo.17724992, last access: February 26, 2026, 2025.

Honkonen, I., Kuvshinov, A., Rastätter, L., and Pulkkinen, A.: Predicting global ground geoelectric field with coupled geospace and three-dimensional geomagnetic induction models, Space Weather, 16, 1028–1041, 10.1029/2018SW001859, 2018.

Huttunen, K. E. J., Koskinen, H. E. J., Pulkkinen, T. I., Pulkkinen, A., Palmroth, M., Reeves, E. G. D., and Singer, H. J.: April 2000 magnetic storm: Solar wind driver and magnetospheric response, J. Geophys. Res., 107(A12), 1440, https://doi.org/10.1029/2001JA009154, 2002.

Jacobsen, K. S., Schultz Beeck, S., Koskimaa, P., Juusola, L., Watson, C., Weygand, J. M., and Durgonics, T.: Scintillation in the Arctic during the May 2024 Mother's Day storm, J. Space Weather Space Clim., 15, 57, https://doi.org/10.1051/swsc/2025045, 2025.

Juusola, L., Kauristie, K., Vanhamäki, H., and Aikio, A.: Comparison of auroral ionospheric and field-aligned currents derived f rom Swarm and ground magnetic field measurements, J. Geophys. Res. Space Physics, 121, 9256–9283, https://doi.org/10.1002/2016JA022961, 2016.

Juusola, L., Vanhamäki, H., Viljanen, A., and Smirnov, M.: Induced currents due to 3D ground conductivity play a major role in the interpretation of geomagnetic variations, Ann. Geophys., 38, 983–998, https://doi.org/10.5194/angeo-38-983-2020, 2020.

Juusola, L., Viljanen, A., Dimmock, A. P., Kellinsalmi, M., Schillings, A., and Weygand, J. M.: Drivers of rapid geomagnetic variations at high latitudes, Ann. Geophys., 41, 13–37, https://doi.org/10.5194/angeo-41-13-2023, 2023a.

Juusola, L., Viljanen, A., Partamies, N., Vanhamäki, H., Kellinsalmi, M., and Walker, S.: Three principal components describe the spatiotemporal development of mesoscale ionospheric equivalent currents around substorm onsets, Ann. Geophys., 41, 483–510, https://doi.org/10.5194/angeo-41-483-2023, 2023b.

Juusola, L., Björnsson, G., Johnsen, M. G., Kauristie, K., Kellinsalmi, M., Matzka, J., Neska, A., Raita, T., Reda, J., Tanskanen, E., Viljanen, A., Willer, A. N., Wittke, J., and Yamauchi, M.: International Monitor for Auroral Geomagnetic Effects (IMAGE) [data set], https://space.fmi.fi/image, last access: February 26, 2026, 2025a.

Juusola, L., Vanhamäki, H., Marshalko, E., Kruglyakov, M., and Viljanen, A.: Estimation of the 3-D geoelectric field at the Earth's surface using Spherical Elementary Current Systems, Ann. Geophys., 43, 271–301, https://doi.org/10.5194/angeo-43-271-2025, 2025b.

Juusola, L., Virtanen, I., Hatch, S. M., Vanhamäki, H., Grandin, M., Partamies, N., Ganse, U., Honkonen, I., Workayehu, A., Kero, A., and Palmroth, M.: An empirical model of high-latitude ionospheric conductances based on EISCAT observations, EGUsphere [preprint], https://doi.org/10.5194/egusphere-2025-2394, 2025c.

Kelbert, A.: The Role of Global/Regional Earth Conductivity Models in Natural Geomagnetic Hazard Mitigation, Surv Geophys, 41, 115–166, https://doi.org/10.1007/s10712-019-09579-z, 2020.

https://doi.org/10.5194/egusphere-2026-1110
Preprint. Discussion started: 13 March 2026

Kelbert, A., Balch, C. C., Pulkkinen, A., Egbert, G. D., Love, J. J., Rigler, E. J., and Fujii, I.: Methodology for time-domain estimation of storm time geoelectric fields using the 3-D magnetotelluric response tensors, Space Weather, 15, 874–894, https://doi.org/10.1002/2017SW001594, 2017.

Kelly, G. S., Viljanen, A., Beggan, C. D., and Thomson, A. W. P.: Understanding GIC in the UK and French high-voltage transmission syste
580 ms during severe magnetic storms, Space Weather, 15, 99–114, https://doi.org/10.1002/2016SW001469, 2017.

Korja, T., Engels, M., Zhamaletdinov, A. A., Kovtun, A. A., Palshin, N. A., Smirnov, M. Y., Tokarev, A. D., Asming, V. E., n, L. L. V., Vardaniants, I. L., and the BEAR Working Group: Crustal conductivity in Fennoscandia — a compilation of a database on crustal conductance in the Fennoscandian Shield, Earth Planets Space, 54, 535–558, https://doi.org/10.1186/BF03353044, 2002.

Kruglyakov, M. and Kuvshinov, A.: Using high-order polynomial basis in 3-D EM forward modeling based on volume integral equation
585 method, Geophysical Journal International, 213, 1387–1401, https://doi.org/10.1093/gji/ggy059, 2018.

Kruglyakov, M., Kuvshinov, A., and Marshalko, E.: Real-time 3-D modeling of the ground electric field due to space weath er events. A concept and its validation., Space Weather, 20, e2021SW002 906, https://doi.org/10.1029/2021SW002906, 2022.

Kruglyakov, M., Marshalko, E., abd M. Smirnov, A. K., and Viljanen, A.: Multi-site transfer function approach for real-time modeling of the gr ound electric field induced by laterally-nonuniform ionospheric source, Space Weather, 21, e2023SW003 621,
590 https://doi.org/10.1029/2023SW003621, 2023.

Laundal, K. M., Yee, J. H., Merkin, V. G., Gjerloev, J. W., Vanhamäki, H., Reistad, J. P., Madelaire, M., Sorathia, K., and Espy, P. J.: Electrojet estimates from mesospheric magnetic field measurements, Journal of Geophysical Research: Space Physics, 126, e2020JA028 644, https://doi.org/10.1029/2020JA028644, 2021.

Lawrence, E., Beggan, C. D., Richardson, G. S., Reay, S., Thompson, V., Clarke, E., Orr, L., Hübert, J., and Smedley, A. R. D.: The
595 geomagnetic and geoelectric response to the May 2024 geomagnetic storm in the United Kingdom, Frontiers in Astronomy and Space Sciences, 12, https://doi.org/10.3389/fspas.2025.1550923, 2025.

Lehtinen, M. and Pirjola, R.: Currents produced in earthed conductor networks by geomagnetically-induced electric fields, Ann. Geophys., 3, 479–484, 1985.

Liu, C., Wang, X., Zhang, S., and Xie, C.: Effects of Lateral Conductivity Variations on Geomagnetically Induced Currents: H-Polarization,
600 IEEE Access, 7, 6310–6318, https://doi.org/10.1109/ACCESS.2018.2889462, 2019.

Love, J. J., Lucas, G. M., Kelbert, A., and Bedrosian, P. A.: Geoelectric hazard maps for the Pacific Northwest, Space Weather, 16, 1114–1127, https://doi.org/10.1029/2018SW001844, 2018.

Love, J. J., Lucas, G. M., Rigler, E. J., Murphy, B. S., Kelbert, A., and Bedrosian, P. A.: Mapping a magnetic superstorm: March 1989 geoelectric hazards and impacts on United States power systems, Space Weather, 20, e2021SW003 030, https://doi.org/10.1029/2021SW003030,
605 2022.

Lucas, G., Love, J. J., Kelbert, A., Bedrosian, P. A., and Rigler, E. J.: A 100-year geoelectric hazard analysis for the U.S. high-voltage power grid, Space Weather, 18, e2019SW002 329, https://doi.org/10.1029/2019SW002329, 2020.

Lyon, R., Richardson, G. S., and Baillie, O.: Long term monitoring of the geoelectric field in the UK - 2012-2024, Geosci. Instrum. Method. Data Syst., 14, 295–310, https://doi.org/10.5194/gi-14-295-2025, 2025.

610 Mac Manus, D. H., Rodger, C. J., Renton, A., Lo, V., Malone-Leigh, J., Petersen, T., Copland, M., Hendry, A. T., Clilverd, M. A., and Richardson, G. S.: Implementing geomagnetically induced currents mitigation during the May 2024 "Gannon" G5 storm: Research informed response by the New Zealand power network, Space Weather, 23, e2025SW004 388, https://doi.org/10.1029/2025SW004388, 2025.

https://doi.org/10.5194/egusphere-2026-1110
Preprint. Discussion started: 13 March 2026

Malone-Leigh, J., Campanyà, J., Gallagher, P. T., Neukirch, M., Hogg, C., and Hodgson, J.: Nowcasting geoelectric fields in Ireland using magnetotelluric transfer functions, J. Space Weather Space Clim., 13, https://doi.org/10.1051/swsc/2023004, 2023.

Malone-Leigh, J., Campanyá, J., Gallagher, P. T., Hodgson, J., and Hogg, C.: Mapping geoelectric field hazards in Ireland, Space Weather, 22, e2023SW003 638, https://doi.org/10.1029/2023SW003638, 2024.

Marsal, S., Torta, J. M., Segarra, A., and Araki, T.: Use of spherical elementary currents to map the polar current systems associated with the geomagnetic sudden commencements on 2013 and 2015 St. Patrick's Day storms, J. Geophys. Res. Space Physics, 122, 194–211, https://doi.org/10.1002/2016JA023166, 2017.

Marsal, S., Torta, J. M., Pavón-Carrasco, F. J., Blake, S. P., and Piersanti, M.: Including the temporal dimension in the SECS technique, Space Weather, 18, e2020SW002 491, https://doi.org/10.1029/2020SW002491, 2020.

Marshalko, E., Kruglyakov, M., Kuvshinov, A., Juusola, L., Kwagala, N. K., Sokolova, E., and Pilipenko, V.: Comparing three approaches to the inducing source setting for the grou nd electromagnetic field modeling due to space weather events, Space Weather, 19, e2020SW002 657, https://doi.org/10.1029/2020SW002657, 2021.

Marshalko, E., Kruglyakov, M., Kuvshinov, A., and Viljanen, A.: Three-dimensional modeling of the ground electric field in Fennoscandia during the Halloween geomagnetic storm, Space Weather, 21, e2022SW003 370, https://doi.org/10.1029/2022SW003370, 2023.

Marshall, R. A., Smith, E. A., Francis, M. J., Waters, C. L., and Sciffer, M. D.: A preliminary risk assessment of the Australian region power network to space weather, Space Weather, 9, https://doi.org/10.1029/2011SW000685, 2011.

McLay, S. A. and Beggan, C. D.: Interpolation of externally-caused magnetic fields over large sparse arrays using Spherical Elementary Current Systems, Ann. Geophys., 28, 1795–1805, https://doi.org/10.5194/angeo-28-1795-2010, 2010.

Michelis, P. D. and Consolini, G.: Unveiling the Gannon Storm: How ground-based magnetometers mapped its global impact, Space Weather, 23, e2025SW004 350, https://doi.org/10.1029/2025SW004350, 2025.

Murphy, B. S., Lucas, G. M., Love, J. J., Kelbert, A., Bedrosian, P. A., and Rigler, E. J.: Magnetotelluric sampling and geoelectric hazard estimation: Are national-scale surveys sufficient?, Space Weather, 19, e2020SW002 693, https://doi.org/10.1029/2020SW002693, 2021.

Ohtani, S., Zou, Y., Merkin, V. G., Wiltberger, M., Pham, K. H., Raptis, S., Friel, M., and Gjerloev, J. W.: Ground magnetic response to an extraordinary IMF BY flip during the May 2024 storm: Travel time from the magnetosheath to dayside high latitudes, Journal of Geophysical Research: Space Physics, 130, e2024JA033 691, https://doi.org/10.1029/2024JA033691, 2025.

Piersanti, M., Oliveira, D. M., D'Angelo, G., Diego, P., Napoletano, G., and Zesta, E.: On the geoelectric field response to the SSC of the May 2024 super storm over Europe, Space Weather, 23, e2024SW004 191, https://doi.org/10.1029/2024SW004191, 2025.

Pirjola, R. J., Boteler, D. H., Tuck, L., and Marsal, S.: The Lehtinen-Pirjola method modified for efficient modelling of geomag netically induced currents in multiple voltage levels of a power network, Ann. Geophys., 40, 205–215, https://doi.org/10.5194/angeo-40-205-2022, 2022.

Pollock, C., Moore, T., Jacques, A., Burch, J., Gliese, U., Saito, Y., Barrie, T. O. L. A. A., Coffey, V., Dorelli, J., Gershman, D., Giles, B., Rosnack, T., Salo, C., Yokota, S., Adrian, M., Aoustin, C., Auletti, C., Aung, S., Bigio, V., Cao, N., Chandler, M., Chornay, D., Christian, K., Clark, G., Collinson, G., Corris, T., Santos, A. D. L., Devlin, R., Diaz, T., Dickerson, T., Dickson, C., Diekmann, A., Diggs, F., Duncan, C., Figueroa-Vinas, A., Firman, C., Freeman, M., Galassi, N., Garcia, K., Goodhart, G., Guererro, D., Hageman, J., Hanley, J., Hemminger, E., Holland, M., Hutchins, M., James, T., Jones, W., Kreisler, S., Kujawski, J., Lavu, V., Lobell, J., LeCompte, E., Lukemire, A., MacDonald, E., Mariano, A., Mukai, T., Narayanan, K., Nguyan, Q., Onizuka, M., Paterson, W., Persyn, S., Piepgrass, B., Cheney, F., Rager, A., Raghuram, T., Ramil, A., Reichenthal, L., Rodriguez, H., Rouzaud, J., Rucker, A., Saito, Y., Samara, M., Sauvaud, J.-A., Schuster, D., Shappirio, M., Shelton, K., Sher, D., Smith, D., Smith, K., Smith, S., Steinfeld, D., Szymkiewicz, R., Tanimoto, K., Taylor,

https://doi.org/10.5194/egusphere-2026-1110
Preprint. Discussion started: 13 March 2026

J., Tucker, C., Tull, K., Uhl, A., Vloet, J., Walpole, P., Weidner, S., White, D., Winkert, G., Yeh, P.-S., and Zeuch, M.: Fast Plasma Investigation for Magnetospheric Multiscale, Space Sci. Rev., 199, 331–406, https://doi.org/10.1007/s11214-016-0245-4, 2016.

Pulkkinen, A., Amm, O., Viljanen, A., and BEAR Working Group: Ionospheric equivalent current distributions determined with the method of spherical elementary current systems, J. Geophys. Res., 108(A2), https://doi.org/10.1029/2001JA005085, 2003a.

Pulkkinen, A., Amm, O., Viljanen, A., and BEAR Working Group: Separation of the geomagnetic variation field on the ground into external and internal parts using the spherical elementary current system method, Earth, Planets and Space, 55, 117–129, https://doi.org/10.1186/BF03351739, 2003b.

Pulkkinen, A., Thomson, A., Clarke, E., and McKay, A.: April 2000 geomagnetic storm: ionospheric drivers of large geomagnetically induced currents, Ann. Geophys., 21, 709–717, https://doi.org/10.5194/angeo-21-709-2003, 2003c.

Pulkkinen, A., Viljanen, A., and Pirjola, R.: Estimation of geomagnetically induced current levels from different input data, Space Weather, 4, S08 005, https://doi.org/10.1029/2006SW000229, 2006.

Pulkkinen, A., Bernabeu, E., Thomson, A., Viljanen, A., Pirjola, R., Boteler, D., Eichner, J., Cilliers, P. J., Welling, D., Savani, N. P., Weigel, R. S., Love, J. J., Balch, C., Ngwira, C. M., Crowley, G., Schultz, A., Kataoka, R., Anderson, B., Fugate, D., Simpson, J. J., and MacAlester, M.: Geomagnetically induced currents: Science, engineering, and applications readiness, Space Weather, 15, 828–856, https://doi.org/10.1002/2016SW001501, 2017.

Ribeiro, J. A., Pinheiro, F. J. G., and Pais, M. A.: First estimations of geomagnetically induced currents in the South of Portugal, Space Weather, 19, e2020SW002 546, https://doi.org/10.1029/2020SW002546, 2021.

Ribeiro, J. A., Pinheiro, F. J. G., Pais, M. A., Santos, R., Cardoso, J., Baltazar-Soares, P., and Santos, F. A. M.: Toward more accurate GIC estimations in the Portuguese power network, Space Weather, 21, e2022SW003 397, https://doi.org/10.1029/2022SW003397, 2023.

Ritter, P., Lühr, H., Viljanen, A., Amm, O., Pulkkinen, A., and Sillanpää, I.: Ionospheric currents estimated simultaneously from CHAMP satellite and IMAGE ground-based magnetic field measurements: a statisticalstudy at auroral latitudes, Ann. Geophys., 22, 417–430, https://doi.org/10.5194/angeo-22-417-2004, 2004.

Rosenqvist, L. and Hall, J. O.: Regional 3-D modeling and verification of geomagnetically induced curr ents in Sweden, Space Weather, 17, 27–36, https://doi.org/10.1029/2018SW002084, 2019.

Rosenqvist, L., Johlander, A., Molenkamp, S., Dimmock, A. P., Setréus, J., and Lanabere, V.: A novel approach for evaluating GIC impacts in the Swedish power grid, Space Weather, 23, e2024SW004 313, https://doi.org/10.1029/2024SW004313, 2025.

Steeb, W., Hardy, Y., and Tanski, I.: Problems and solutions for Groups, Lie groups, Lie algebras with applications, World Scientific Publishing Company, ISBN 9789813104112, https://books.google.fi/books?id=UdI7DQAAQBAJ, 2012.

Untiedt, J. and Baumjohann, W.: Studies of polar current systems using the IMS Scandinavian magnetometer array, Space Science Reviews, 63, 245–390, https://doi.org/10.1007/BF00750770, 1993.

Vanhamäki, H. and Juusola, L.: Introduction to Spherical Elementary Current Systems, in: Ionospheric Multi-Spacecraft Analysis Tools, pp. 5–33, ISSI Scientific Report Series 17, https://doi.org/10.1007/978-3-030-26732-2_13, 2020.

Vanhamäki, H., Viljanen, A., Pirjola, R., and Amm, O.: Deriving the geomagnetically induced electric field at the Earth's sur face from the time derivative of the vertical magnetic field, Earth, Planets and Space, 65, 997–1006, https://doi.org/10.5047/eps.2013.03.013, 2013.

Viljanen, A.: Relation of geomagnetically induced currents and local geomagnetic var iations, in: IEEE Transactions on Power Delivery, vol. 13, 4, pp. 1285–1290, https://doi.org/10.1109/61.714497, 1998.

Viljanen, A. and Pirjola, R.: Geomagnetically induced currents in the Finnish high-voltage power system - a geophysical review, Surv. Geophys., 15, 383–408, https://doi.org/10.1007/BF00665999, 1994.

https://doi.org/10.5194/egusphere-2026-1110
Preprint. Discussion started: 13 March 2026

690 Viljanen, A., Nevanlinna, H., Pajunpää, K., and Pulkkinen, A.: Time derivative of the horizontal geomagnetic field as an activity indicator, Ann. Geophys., 19, 1107–1118, https://doi.org/10.5194/angeo-19-1107-2001, 2001.

Viljanen, A., Pulkkinen, A., Amm, O., Pirjola, R., Korja, T., and Group, B. W.: Fast computation of the geoelectric field using the method of elementary current systems and planar Earth models, Ann. Geophys., 22, 101–113, https://doi.org/10.5194/angeo-22-101-2004, 2004.

Viljanen, A., Pirjola, R., Wik, M., Ádám, A., Prácser, E., Sakharov, Y., and Katkalov, J.: Continental scale modelling of geomagnetically
695 induced currents, J. Space Weather Space Clim., 2, A17, https://doi.org/10.1051/swsc/2012017, 2012.

Viljanen, A., Pirjola, R., Prácser, E., Katkalov, J., and ik, M. W.: Geomagnetically induced currents in Europe - Modelled occurrence in a continent-wide power grid, J. Space Weather Space Clim., 4, A09, https://doi.org/10.1051/swsc/2014006, 2014.

Viljanen, A., Marshalko, E., Juusola, L., Laitinen, T., and Kauristie, K.: Comparison of the modelled geoelectric fields of the Carrington and Halloween storms, J. Space Weather Space Clim., 16, 4, https://doi.org/10.1051/swsc/2025058, 2026.

700 Wallner, A. V. L., Dimmock, A. P., Lanabere, V., Johlander, A., Molenkamp Venholen, S., Viljanen, A., Juusola, L., Rosenqvist, L., Setréus, J., Yordanova, E., Buchert, S., Heiter, U., and Khotyaintsev, Y. V.: The geomagnetic storm on 10-12 May 2024 and its effect on the Swedish power grid, Space Weather, 24, e2025SW004 788, https://doi.org/10.1029/2025SW004788, 2026.

Weiler, E., Möstl, C., Davies, E. E., Veronig, A. M., Amerstorfer, U. V., Amerstorfer, T., Louëdec, J. L., Bauer, M., Lugaz, N., Haberle, V., Rüdisser, H. T., Majumdar, S., and Reiss, M.: First observations of a geomagnetic superstorm with a sub-L1 monitor, Space Weather, 23,
705 e2024SW004 260, https://doi.org/10.1029/2024SW004260, 2025.

Weygand, J. M., Amm, O., Viljanen, A., Angelopoulos, V., Murr, D., Engebretson, M. J., Gleisner, H., and Mann, I.: Application and validation of the spherical elementary currents systems technique for deriving ionospheric equivalent currents with the North American and Greenland ground magnetometer arrays, J. Geophys. Res., 116, https://doi.org/10.1029/2010JA016177, 2011.

World Data Center for Geomagnetism, Kyoto, Imajo, S., Matsuoka, A., Toh, H., and Iyemori, T.: Mid-latitude Geomagnetic Indices ASY
710 and SYM (ASY/SYM Indices) [data set], https://wdc.kugi.kyoto-u.ac.jp, https://doi.org/10.14989/267216, last access: February 26, 2026, 2022.

https://doi.org/10.5194/egusphere-2026-1110
Preprint. Discussion started: 13 March 2026

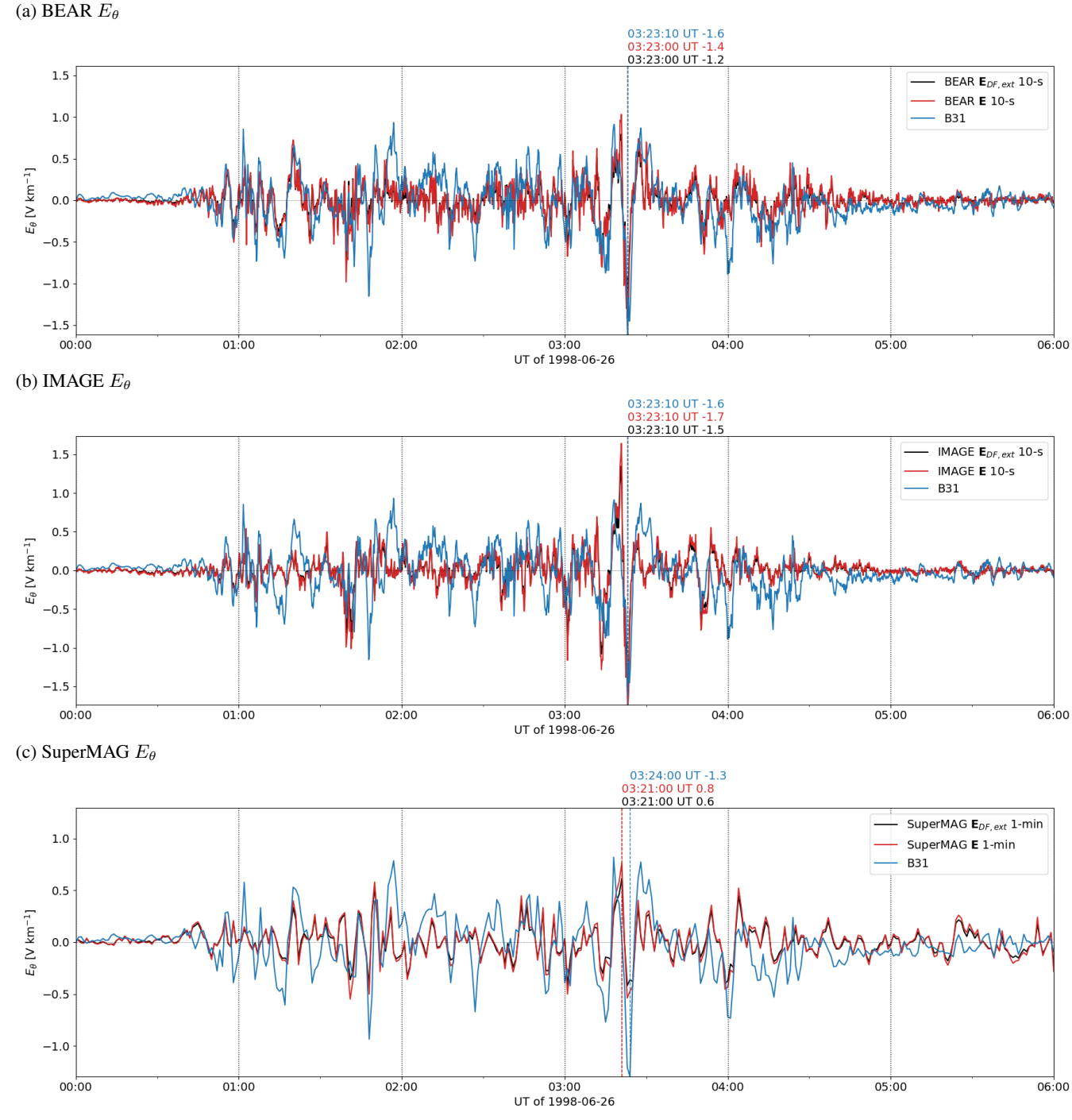

Figure 2. South component of the geoelectric field at the Earth's surface (E_θ) on 26 June 1998 between 00:00:00 and 06:00:00 UT. The blue curve is the measured E_θ at station B31 of the BEAR network (10 s data in (a) and (b), 1 min average in (c)), the black curve is $E_{DF,\theta}$ estimated from BEAR (a), IMAGE (b), or SuperMAG (c) magnetometer measurements using the SECS method, and the red curve is the total modelled E_θ, estimated from $\boldsymbol{E}_{DF}$ using Eq. 5–6. The epoch of the maximum value for each curve is indicated by the labeled vertical line.

https://doi.org/10.5194/egusphere-2026-1110
Preprint. Discussion started: 13 March 2026

(a) BEAR E_ϕ

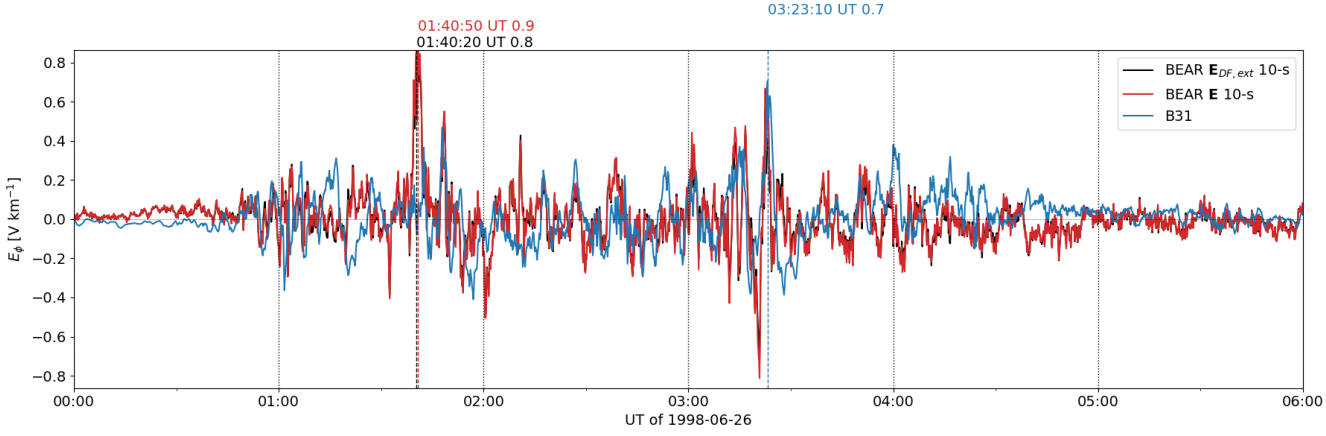

(b) IMAGE E_ϕ

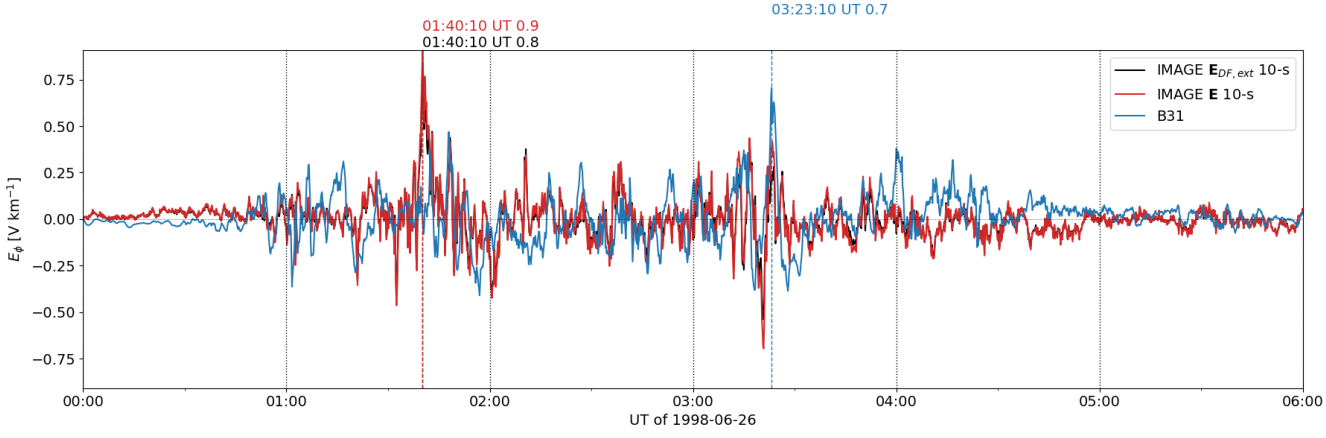

(c) SuperMAG E_ϕ

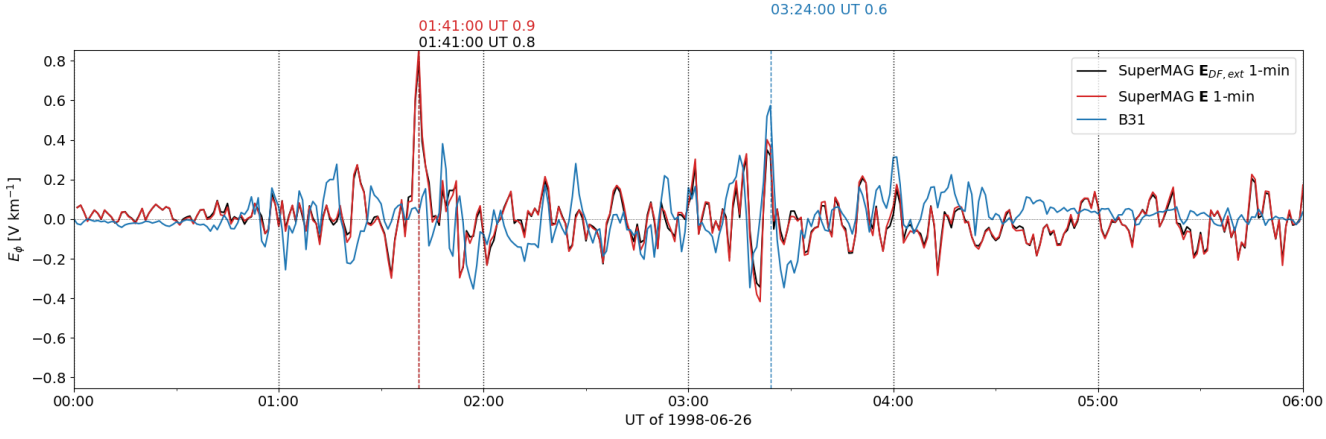

Figure 3. The same as Fig. 2 except for the east component of the geoelectric field (E_ϕ) instead of the south component.

https://doi.org/10.5194/egusphere-2026-1110
Preprint. Discussion started: 13 March 2026

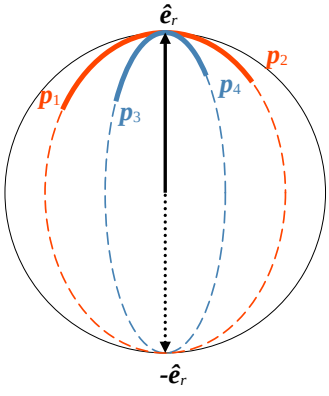

Figure 4. The power line between points $\boldsymbol{p}_1$ and $\boldsymbol{p}_2$ and the grid cell edge between points $\boldsymbol{p}_3$ and $\boldsymbol{p}_4$ were assumed to follow great circle arcs. Their intersection points $\hat{\boldsymbol{e}}_r$ and $-\hat{\boldsymbol{e}}_r$ were found by calculating the normalized cross product $\hat{\boldsymbol{e}}_r = \boldsymbol{r}/|\boldsymbol{r}|$ between the normal vectors of the two great circle planes $\boldsymbol{r} = (\boldsymbol{p}_1 \times \boldsymbol{p}_2) \times (\boldsymbol{p}_3 \times \boldsymbol{p}_4)$. From the two alternative crossing points $\hat{\boldsymbol{e}}_r$ and $-\hat{\boldsymbol{e}}_r$, the point along the power line was selected by requiring that the power line length $l_{\boldsymbol{p}_1\boldsymbol{p}_2} = l_{\boldsymbol{p}_1\hat{\boldsymbol{e}}_r} + l_{\boldsymbol{p}_2\hat{\boldsymbol{e}}_r}$.

https://doi.org/10.5194/egusphere-2026-1110
Preprint. Discussion started: 13 March 2026

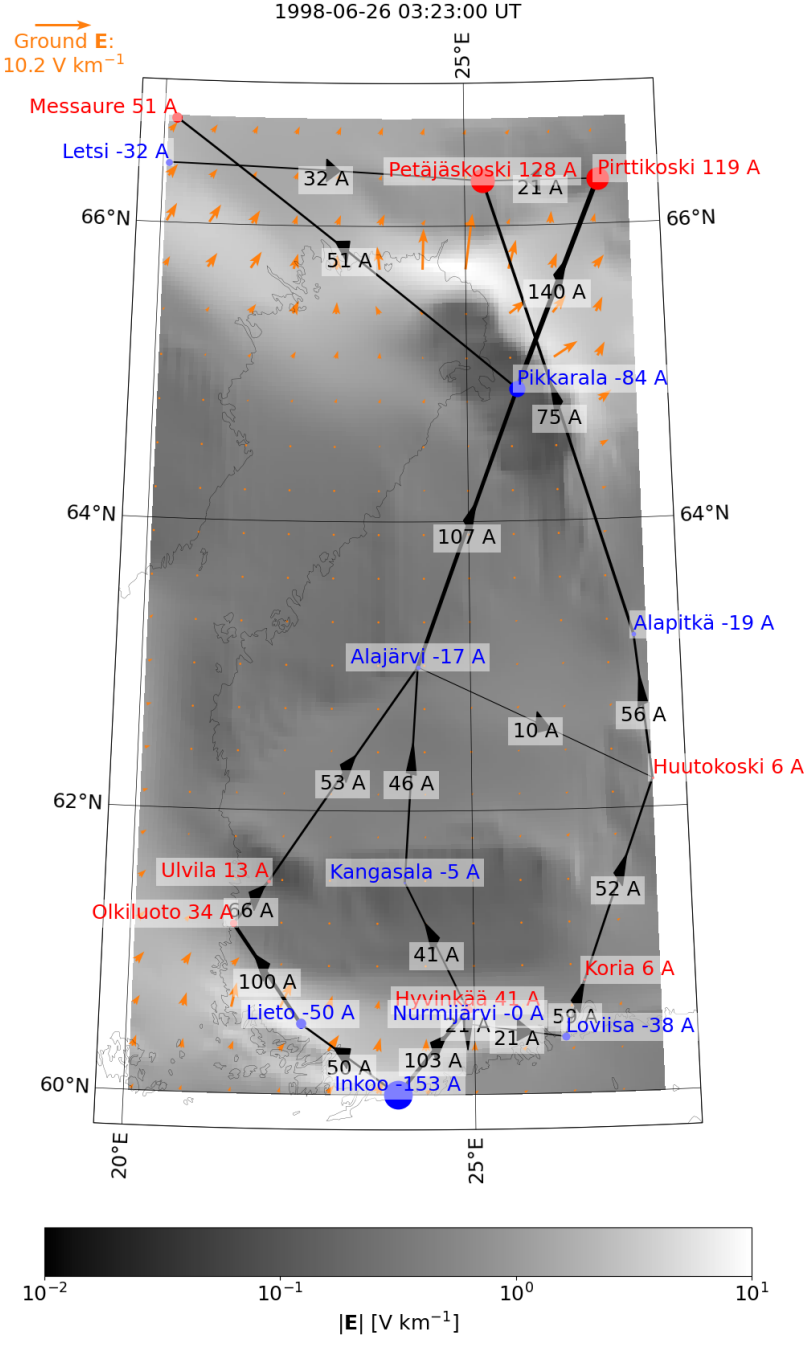

https://doi.org/10.5194/egusphere-2026-1110
Preprint. Discussion started: 13 March 2026

Figure 5. GIC in the Finnish benchmark power grid on 26 June 1998 at 03:23:00 UT as driven by the total electric field estimated from BEAR magnetometer data using the SECS methods and Eq. 5–6. The total electric field in the grid area is shown by the orange arrows (only every 10th arrow is shown for clarity) and its intensity by the background color. The powerlines are shown in black, and the black arrows with labels in the middle of each line indicate the amplitude and direction of current in each powerline. The labeled circles illustrate the amplitude of the current entering and leaving the power grid at each named substation. Blue color indicates current direction from ground to power grid and red color from power grid to ground. The size of the symbol at each substations is scaled according to the amount of GIC. Similarly, the relative thickness of the powerlines indicates the amount of current flow in the line.

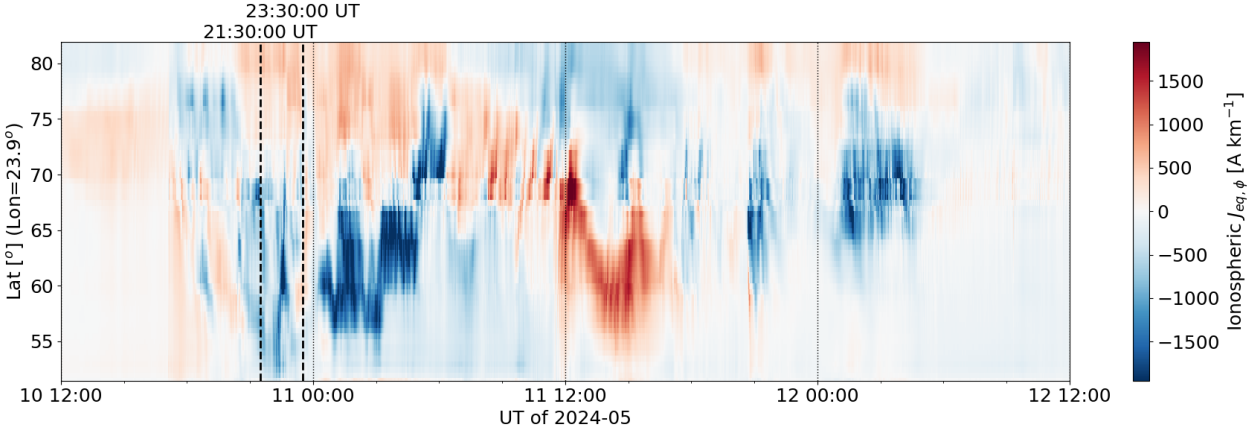

Figure 6. Latitude profiles of the east component of the ionospheric equivalent current density at 23.9^o longitude between 10 May 2024 12:00 UT and 12 May 2024 12:00 UT, derived from IMAGE data. The two-hour time interval studied in more detail is indicated by the vertical lines.

https://doi.org/10.5194/egusphere-2026-1110
Preprint. Discussion started: 13 March 2026

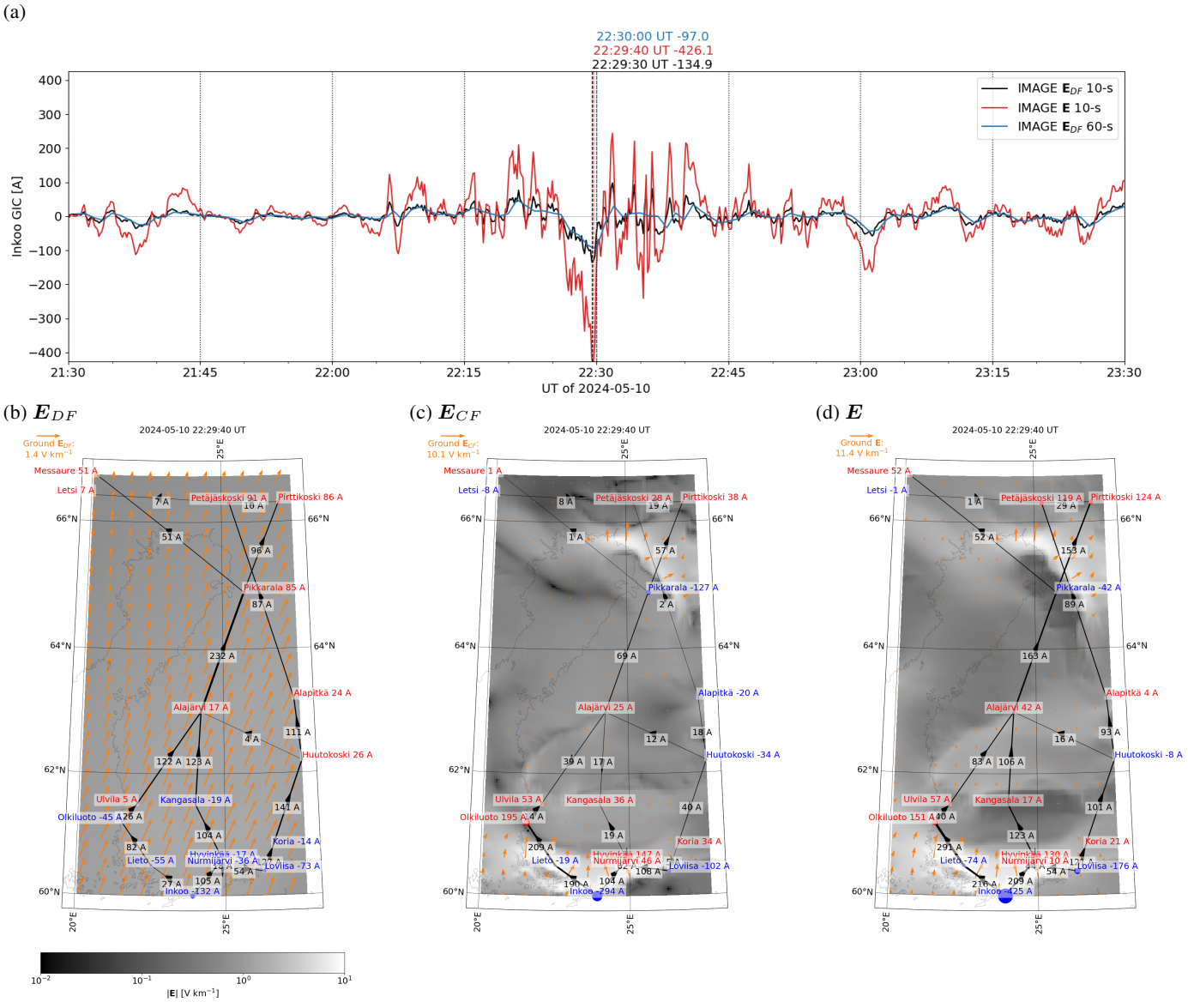

Figure 7. (a): Time series of GIC at Inkoo substation calculated using the total geoelectric field and the DF component of the geoelectric field estimated from 10 s IMAGE observations and using the DF component of the geoelectric field estimated from 1 min averaged IMAGE observations. The peak values and their amplitudes are indicated by the labeled vertical lines. (b): GIC in the Finnish benchmark power grid on 10 May 2024 at 22:29:40 UT in a format similar to Fig. 5, calculated from the DF component of the geoelectric field estimated using 10 s IMAGE observations. (c): The same as (b) except for the CF component of the geoelectric field instead of the DF component. (d): The same as (b) except for the total geoelectric field instead of the DF component. The substation symbol sizes and power line widths in the three panels have been scaled so that they are comparable.

https://doi.org/10.5194/egusphere-2026-1110
Preprint. Discussion started: 13 March 2026

(a)

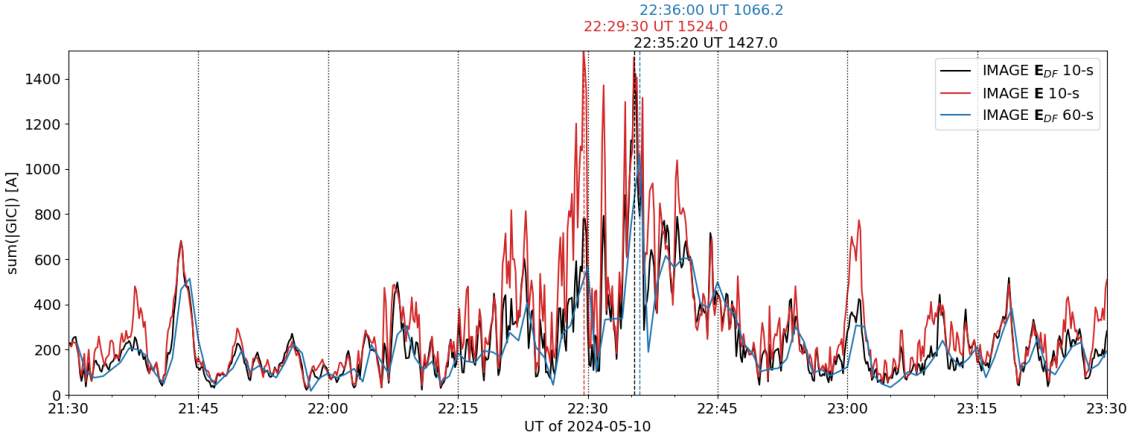

(b) Power grid shifted 1^o northward

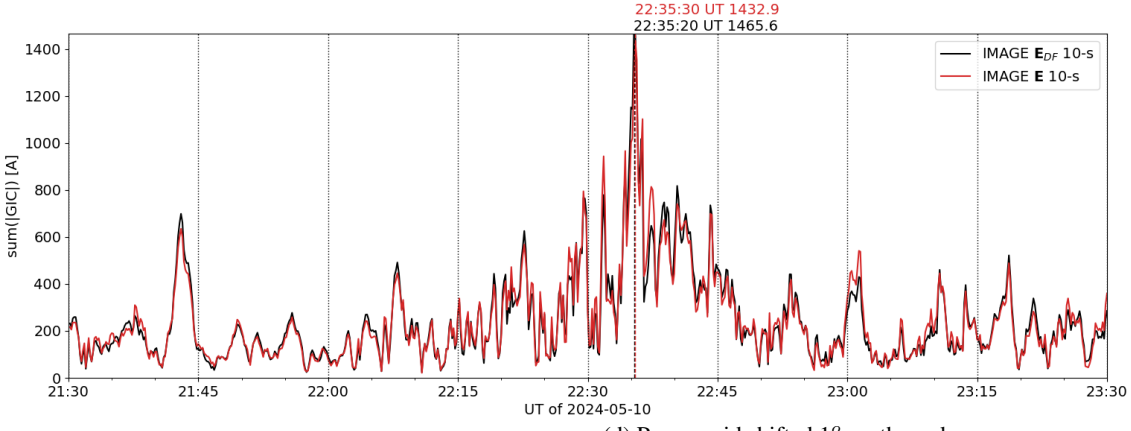

(c)

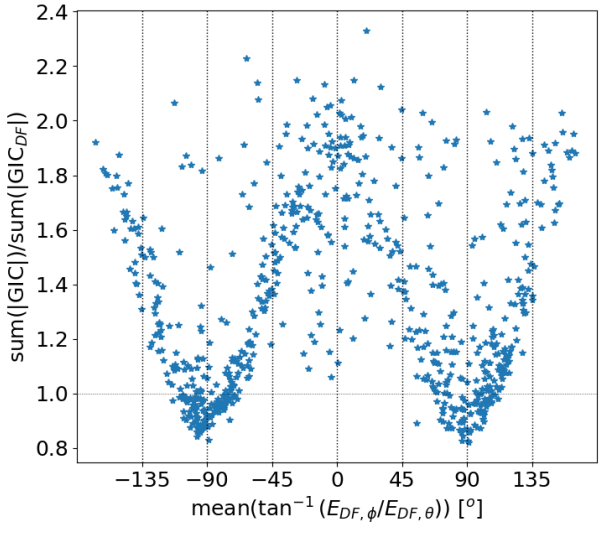

(d) Power grid shifted 1^o northward

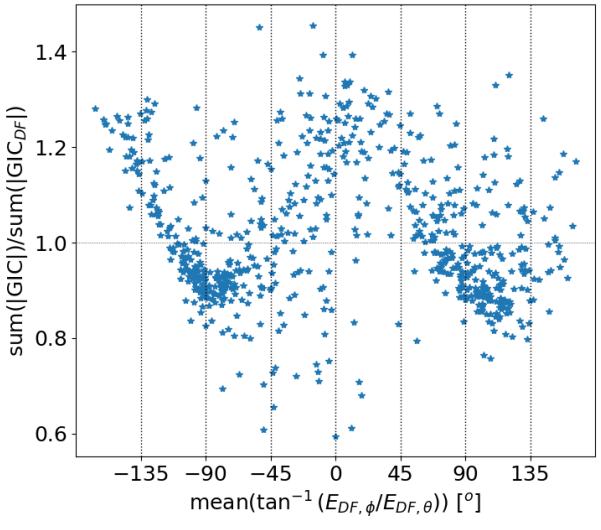

https://doi.org/10.5194/egusphere-2026-1110
Preprint. Discussion started: 13 March 2026

Figure 8. (a): The same as Fig. 7a except that instead of GIC at one substation, the sum of absolute values of GIC at all substations of the power grid is shown. (b): The same as (a) except that the power grid has been shifted 1^o northward in latitude and the 1 min curve is not shown. (c): Relative GIC sum calculated using $\boldsymbol{E}$ and $\boldsymbol{E}_{DF}$ as a function of average $\boldsymbol{E}_{DF}$ direction in the network area. The directon angle 0^o means southward $\boldsymbol{E}_{DF}$ and 90^o means eastward $\boldsymbol{E}_{DF}$. (d): Otherwise the same as (c) except for the power grid that has been shifted 1^o northward in latitude.

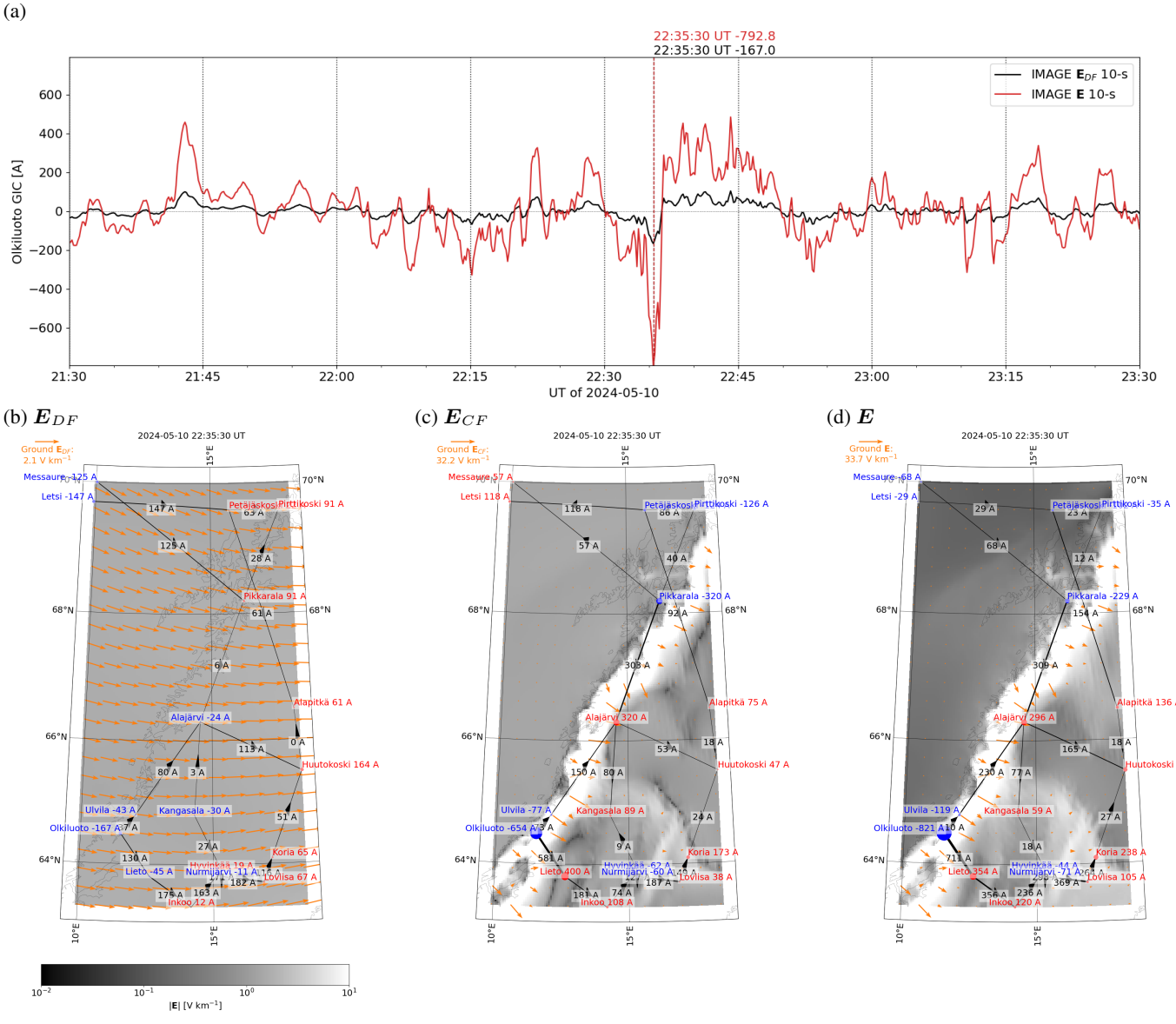

Figure 9. The same as Fig. 7 except for Olkiluoto substation, instead of Inkoo. The power grid has been shifted to the Norwegian coast such that Olkiluoto lies at 64.5^o latitude and 11.5^o longitude. The power grid geometry has been kept intact in the shift.

https://doi.org/10.5194/egusphere-2026-1110
Preprint. Discussion started: 13 March 2026

(a)

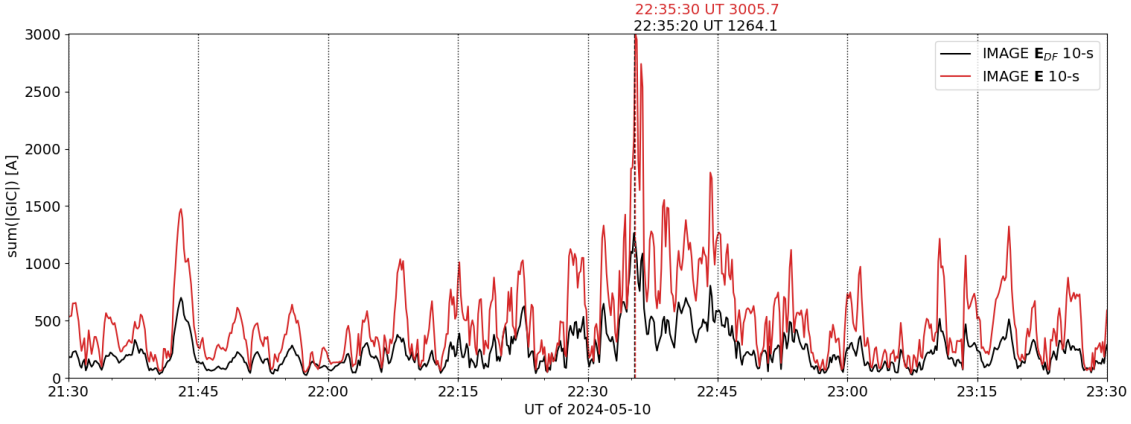

(b)

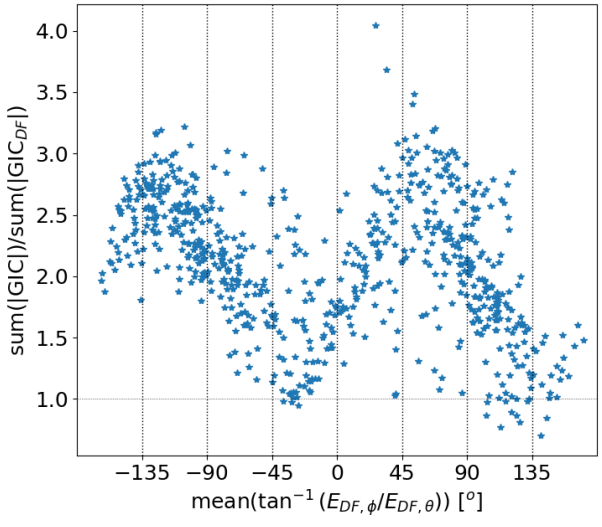

Figure 10. The same as Fig. 8b and 8d, except that the power grid has been shifted to the Norwegian coast.

https://doi.org/10.5194/egusphere-2026-1110
Preprint. Discussion started: 13 March 2026

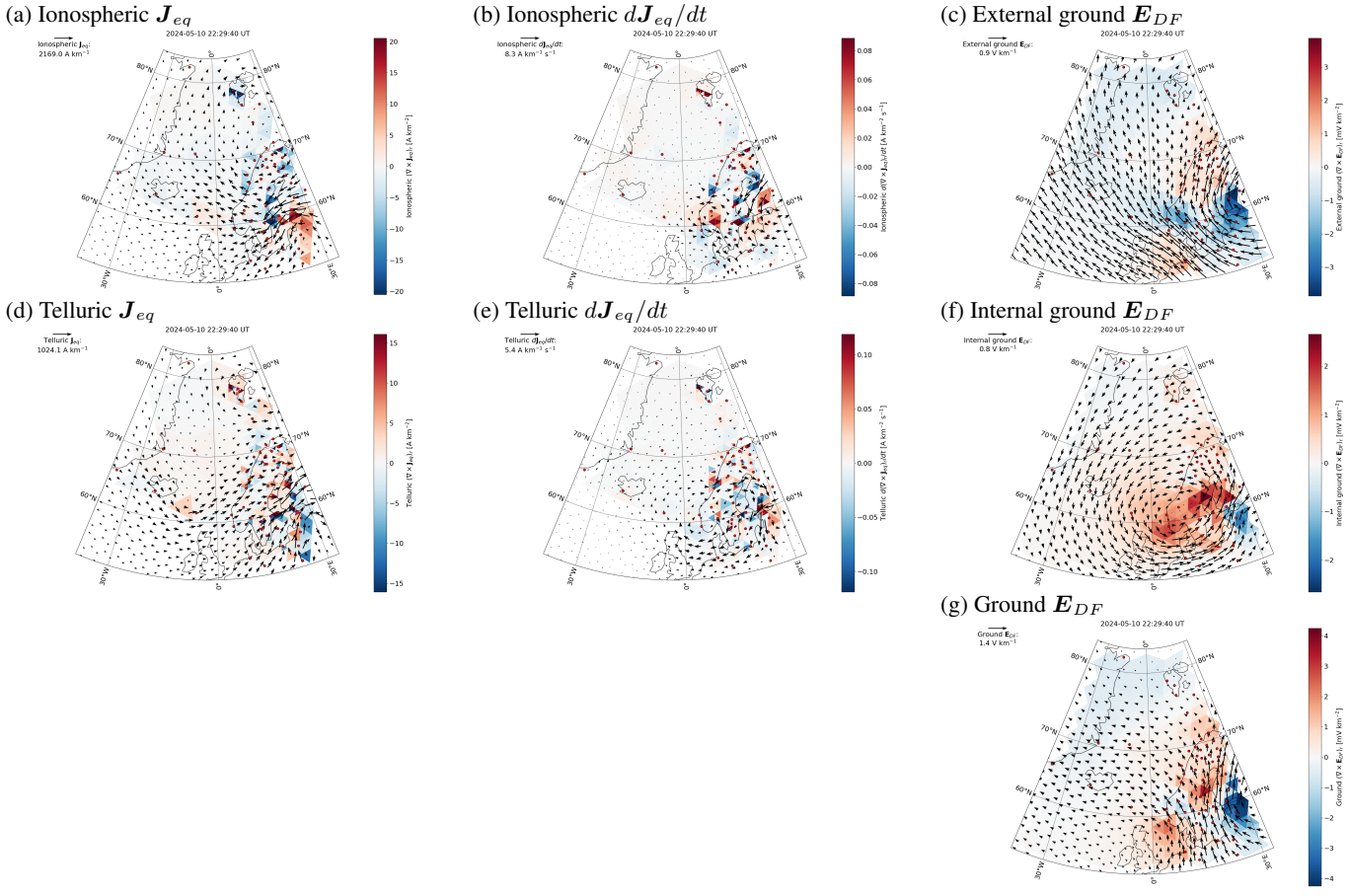

Figure 11. (a): Ionospheric equivalent current density (arrows) and its curl (color) on 10 May 2024 at 22:29:40 UT, derived from 10 s IMAGE magnetometer observations (red dots). (b): Time derivative of the ionospheric equivalent current density and its curl. (c): External DF component of the geoelectric field (arrows) and its curl (color) on the ground. (d): Telluric equivalent current density and its curl. (e): Time derivative of the telluric equivalent current density and its curl. (f): Internal DF component of the geoelectric field (arrows) and its curl (color) on the ground. (g): DF component of the geoelectric field on the ground.

https://doi.org/10.5194/egusphere-2026-1110
Preprint. Discussion started: 13 March 2026

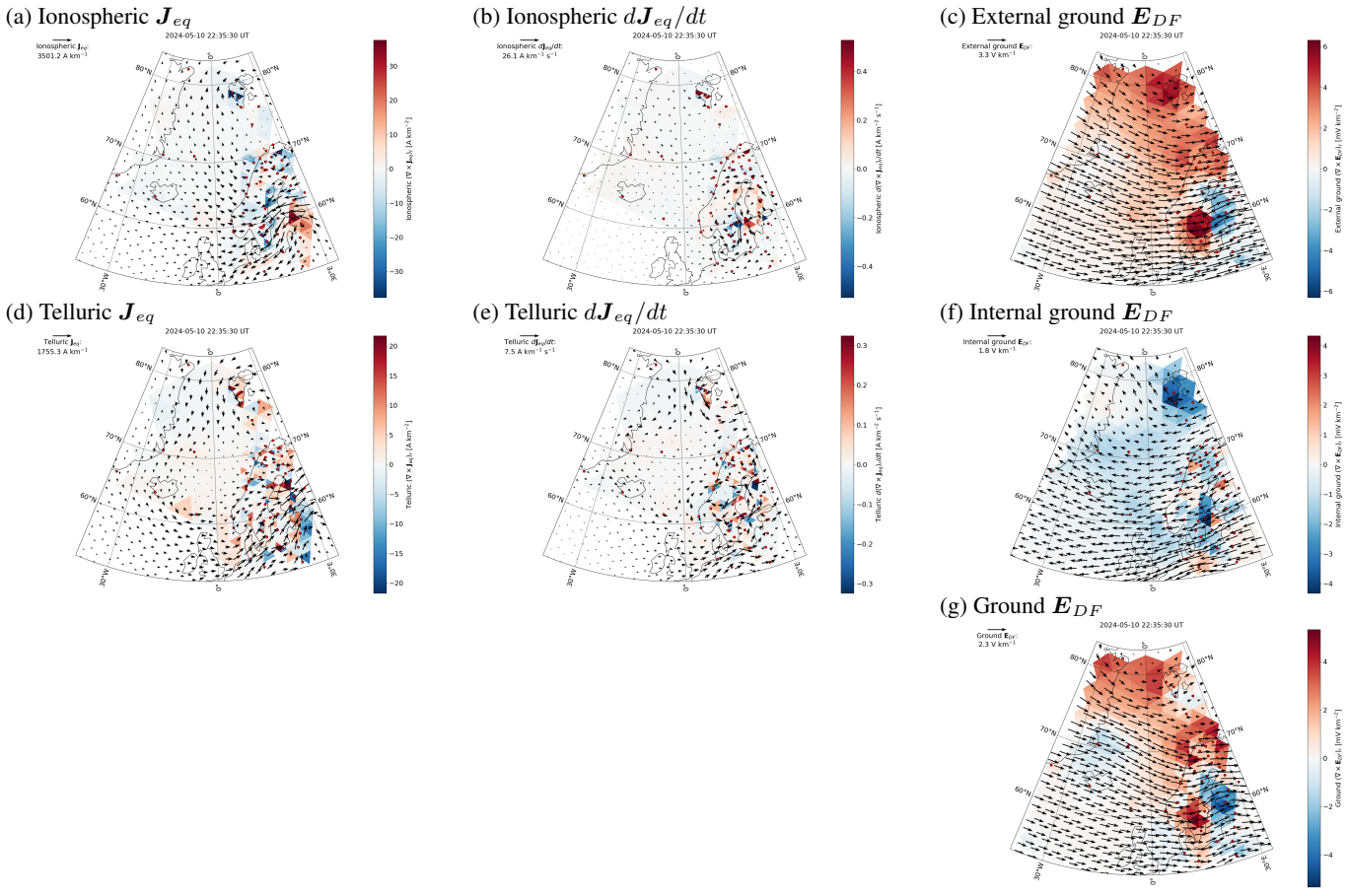

Figure 12. The same as Fig. 11 except for Olkiluoto substation (shifted to the Norwegian coast) GIC peak time instead of Inkoo GIC peak time.

https://doi.org/10.5194/egusphere-2026-1110
Preprint. Discussion started: 13 March 2026

(a) E_θ

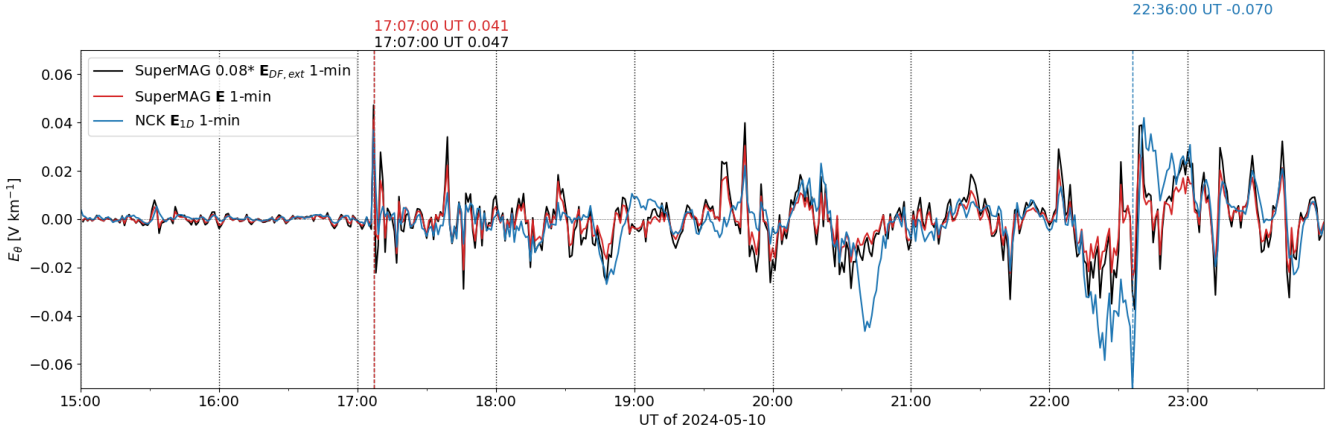

(b) E_ϕ

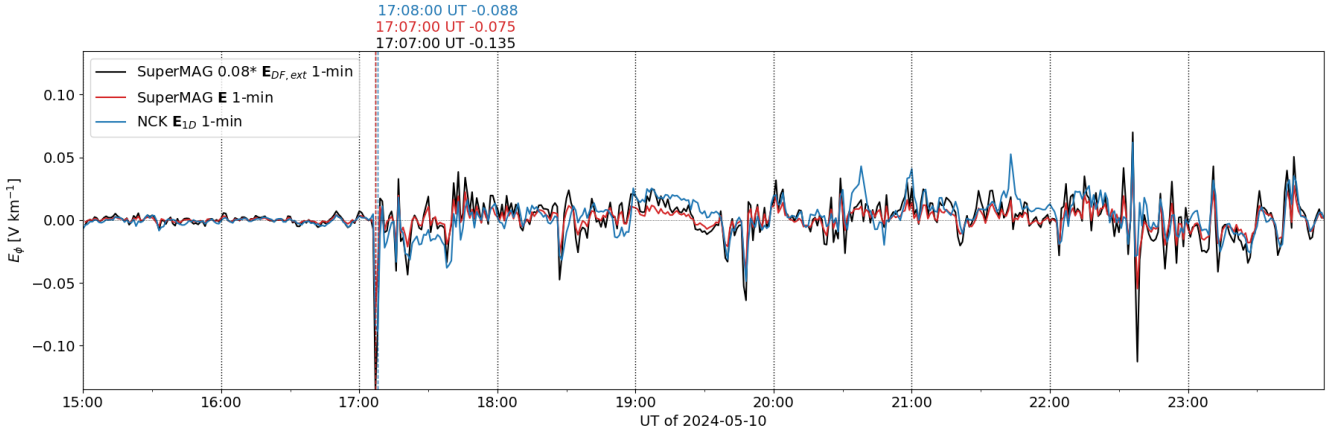

(c) $|\boldsymbol{E}|$

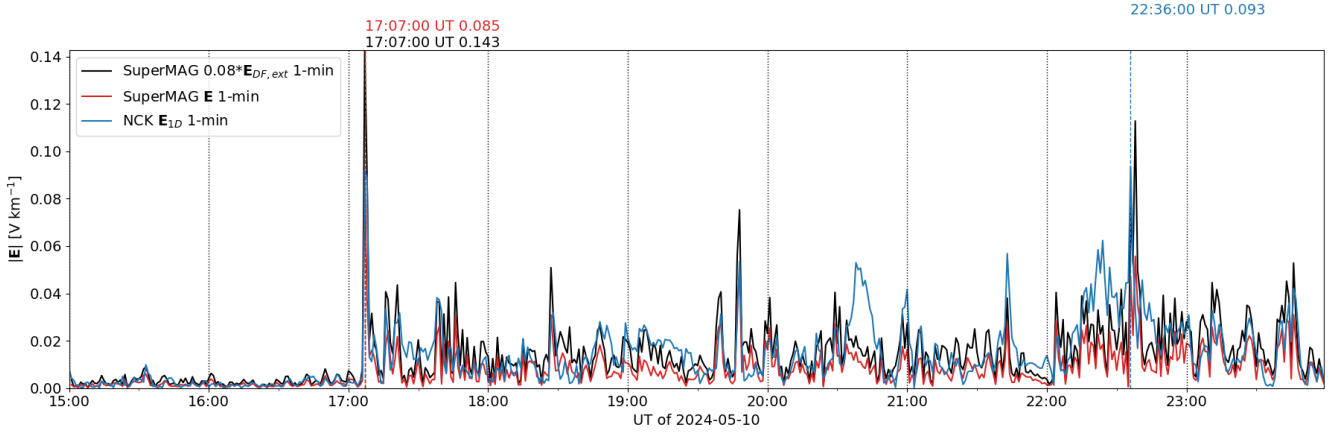

https://doi.org/10.5194/egusphere-2026-1110
Preprint. Discussion started: 13 March 2026

Figure 13. Comparison of modelled geoelectric fields at Nagycenk (NCK; 47.63^o latitude and 16.72^o longitude), Hungary, on 10 May 2024 from 15:00:00 to 23:59:00 UT. The external part of $\boldsymbol{E}_{DF}$ has been calculated from SuperMAG magnetometer data using spherical elementary current systems. $\boldsymbol{E}_{1D}$ has been calculated from local magnetic variations and a 1-D ground conductivity model. At NCK, 1-D modelling has been shown to reproduce the measured geoelectric field very well (Viljanen et al., 2012). (a): South component of the geoelectric field. (b): East component of the geoelectric field. (c): Amplitude of the geoelectric field.

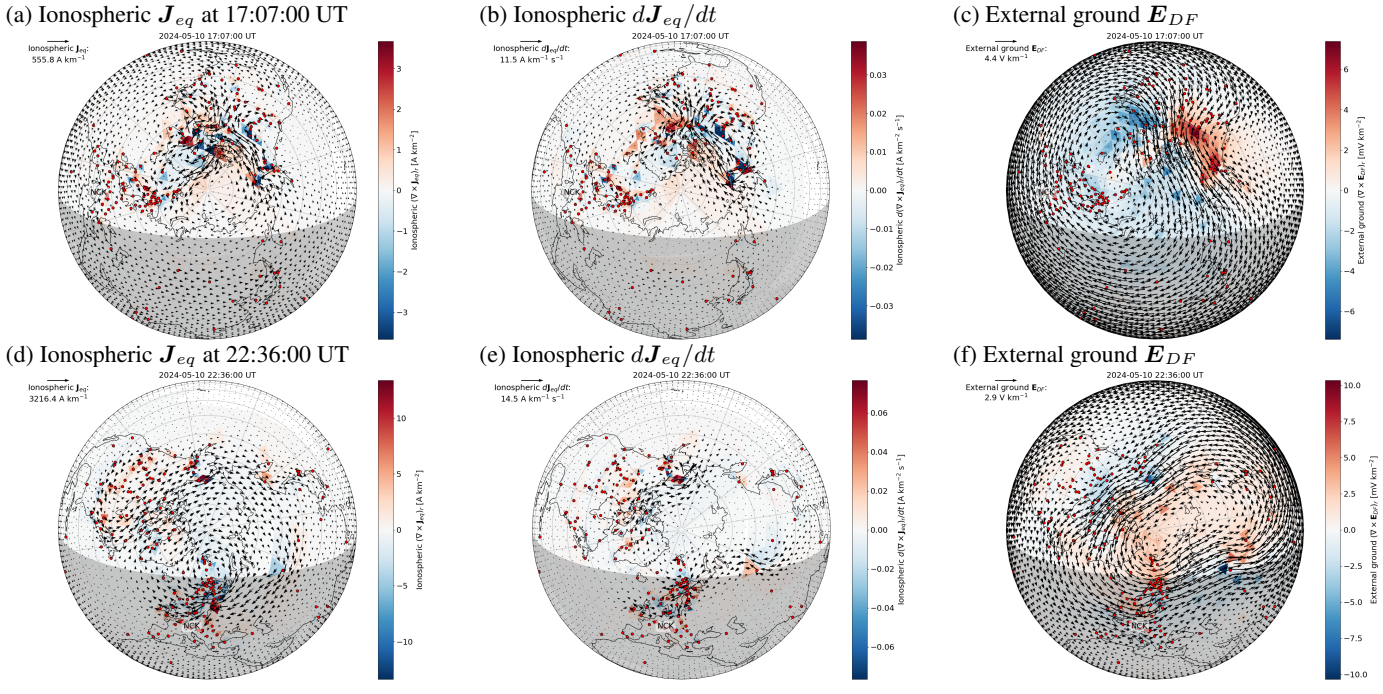

Figure 14. The same as Fig. 11a–c except that global 1 min SuperMAG data are used instead of regional 10 s IMAGE data and the time is 17:07:00 (a–c) or 22:36:00 UT (d–e) instead of 22:29:30 UT. The maps are oriented such that noon is at the top, and the nightside is shaded.

https://doi.org/10.5194/egusphere-2026-1110
Preprint. Discussion started: 13 March 2026

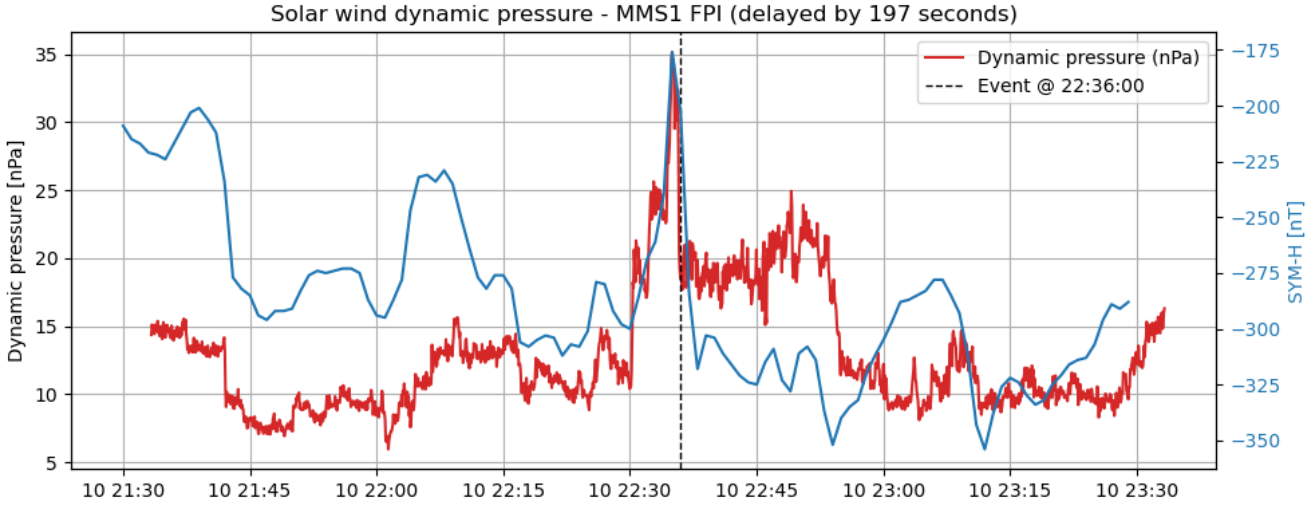

Figure 15. Solar wind dynamic pressure observed by MMS1 satellite upstream of the Earth and SYM-H index. MMS1 data have been delayed by 197 s to match the peak times of the solar wind dynamic pressure and SYM-H. The vertical line indicates the peak time of $|\boldsymbol{E}_{1D}|$.

https://doi.org/10.5194/egusphere-2026-1110
Preprint. Discussion started: 13 March 2026

(a) Icosahedron

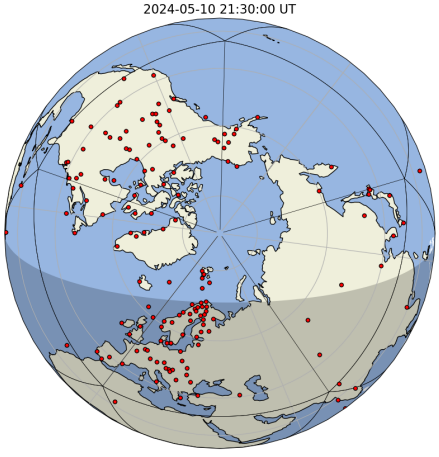

(b) 1. refinement

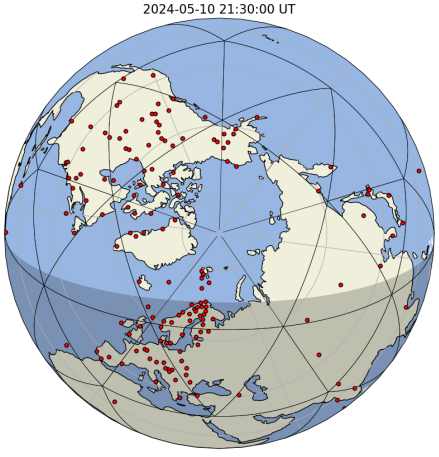

(c) 2. refinement

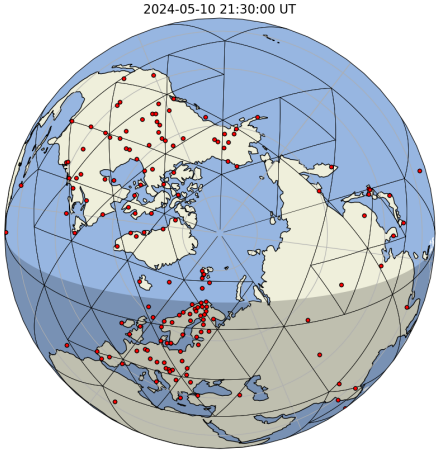

(d) Last refinement

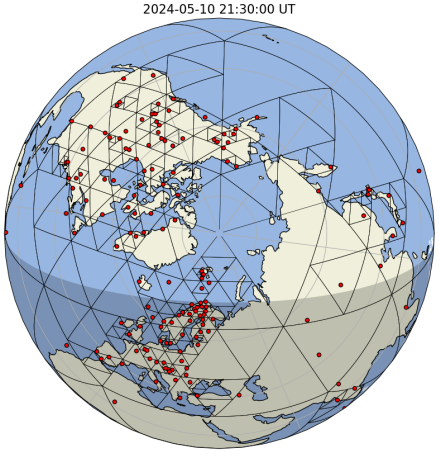

(e) Additional refinement (SECS grid)

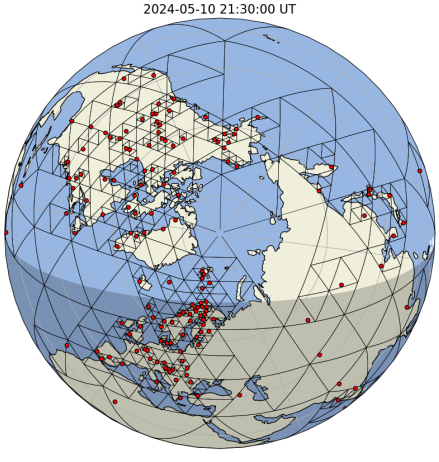

(f) Uniform output grid

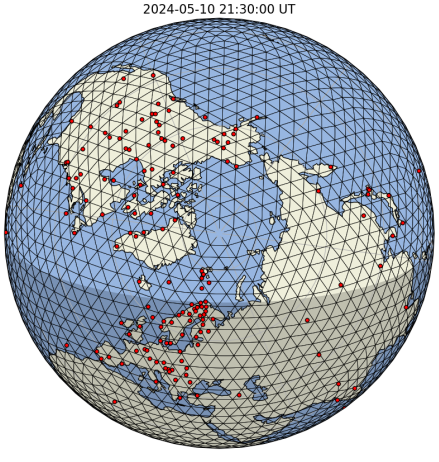

https://doi.org/10.5194/egusphere-2026-1110
Preprint. Discussion started: 13 March 2026

Figure A1. Creation of a global triangular grid for the SECS method, adapted to SuperMAG magnetometer density on 10 May 2024 at 21:30:00 UT. (a): The starting point is an icosahedron. (b): 1. refinement: All triangular cells containing more than one magnetometer are split into four cells. (c): 2. refinement. (d): Last refinement. Now there is at most one magnetometer inside each cell. (e): Additional refinement of all cells containing a magnetometer. Minimum triangle side length is now 28 km. This grid is used for the DF SECS poles. (f): Uniform output grid. Minimum triangle side length is 447 km.

(a) IMAGE SECS grid

(b) IMAGE output grid

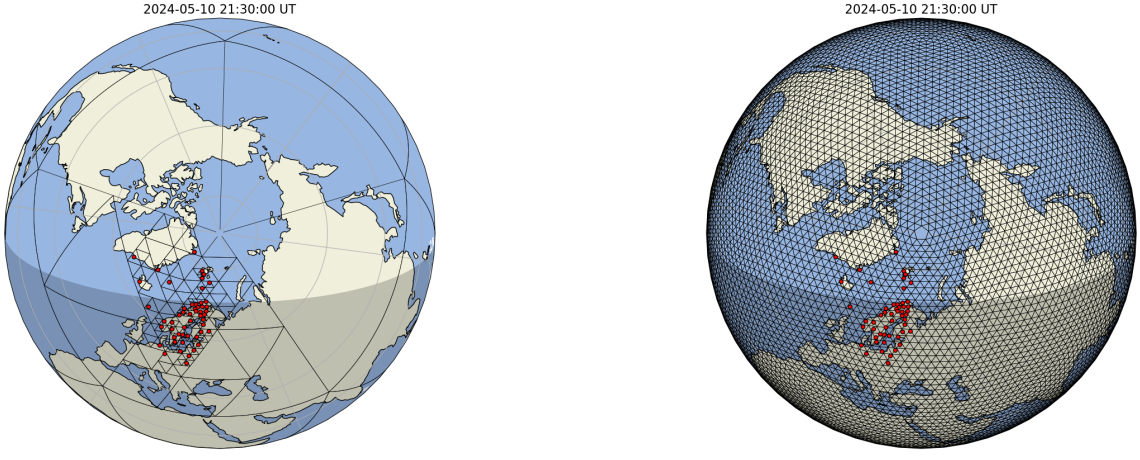

Figure A2. (a): Adapted triangular grid used for the DF SECS poles when analysing regional IMAGE data on 10 May 2024 at 21:30:00 UT. Minimum triangle side length is 28 km. (b): The uniform output grid is one adaptation level denser than the one used for global SuperMAG data (Fig. A1f). Its minimum triangle side length is 224 km.